Chem

CellPress

Article

Transition-Metal Single Atoms in a Graphene Shell as Active Centers for Highly Efficient Artificial Photosynthesis

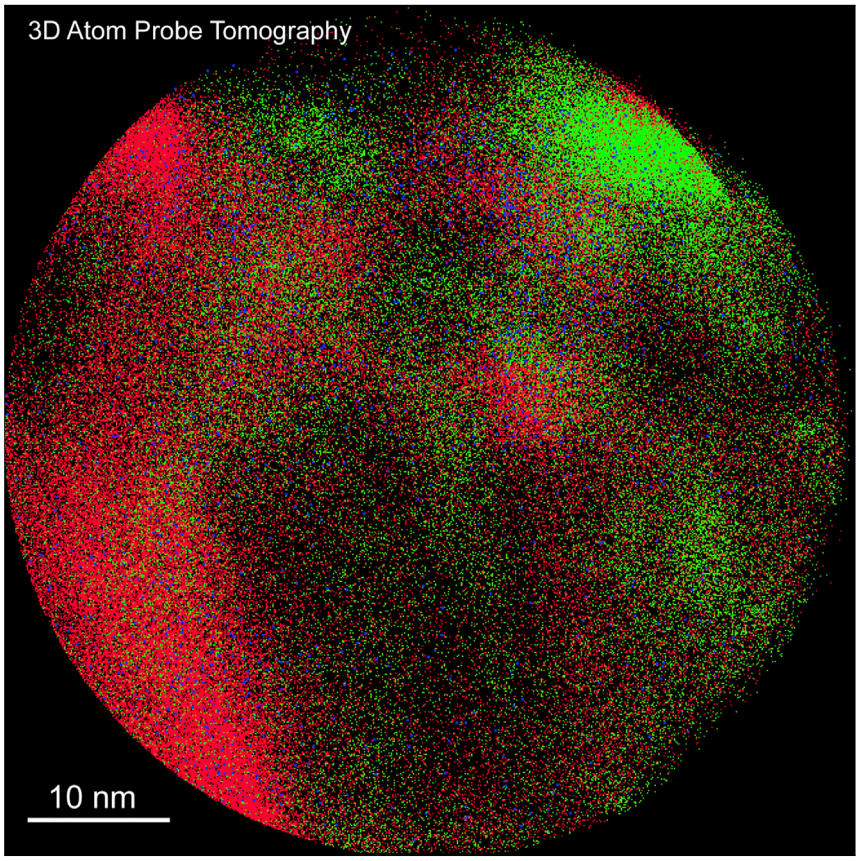

State-of-the-art three-dimensional atom probe tomography provides direct evidence of Ni single atoms coordinated in graphene vacancies for highly selective CO_2 reduction to CO and suppressed hydrogen evolution in water.

Kun Jiang, Samira Siahrostami, Austin J. Akey, ..., Jens K. Nørskov, Yi Cui, Haotian Wang

hwang@rowland.harvard.edu

HIGHLIGHTS

Single Ni atoms coordinated in graphene exhibit superb catalytic CO_2RR performance

Atomic-resolution 3D APT provides direct identification of single Ni atoms

DFT simulations suggest that the tuning of electronic structure favors CO_2RR over HER

Jiang et al., Chem 3, 1–11
December 14, 2017
https://doi.org/10.1016/j.chempr.2017.09.014

Please cite this article in press as: Jiang et al., Transition-Metal Single Atoms in a Graphene Shell as Active Centers for Highly Efficient Artificial Photosynthesis, Chem (2017), https://doi.org/10.1016/j.chempr.2017.09.014

Chem

CellPress

Article

Transition-Metal Single Atoms in a Graphene Shell as Active Centers for Highly Efficient Artificial Photosynthesis

Kun Jiang,[1,11] Samira Siahrostami,[2,11] Austin J. Akey,[3] Yanbin Li,[4] Zhiyi Lu,[4] Judith Lattimer,[5] Yongfeng Hu,[6] Chris Stokes,[1] Mahesh Gangishetty,[1] Guangxu Chen,[4] Yawei Zhou,[7] Winfield Hill,[1] Wen-Bin Cai,[7] David Bell,[3,8] Karen Chan,[9] Jens K. Nørskov,[2,9] Yi Cui,[3,10] and Haotian Wang[1,12,*]

SUMMARY

Utilizing solar energy to fix CO_2 with water into chemical fuels and oxygen, a mimic process of photosynthesis in nature, is becoming increasingly important but still challenged by low selectivity and activity, especially in CO_2 electrocatalytic reduction. Here, we report transition-metal atoms coordinated in a graphene shell as active centers for aqueous CO_2 reduction to CO with high faradic efficiencies over 90% under significant currents up to ~60 mA/mg. We employed three-dimensional atom probe tomography to directly identify the single Ni atomic sites in graphene vacancies. Theoretical simulations suggest that compared with metallic Ni, the Ni atomic sites present different electronic structures that facilitate CO_2-to-CO conversion and suppress the competing hydrogen evolution reaction dramatically. Coupled with Li^+-tuned Co_3O_4 oxygen evolution catalyst and powered by a triple-junction solar cell, our artificial photosynthesis system achieves a peak solar-to-CO efficiency of 12.7% by using earth-abundant transition-metal electrocatalysts in a pH-equal system.

INTRODUCTION

Effectively converting clean solar energy into carbon fuels via electrocatalytic carbon dioxide (CO_2) reduction and water oxidation, a mimic process of photosynthesis in nature, can potentially play a critical role in sustaining the global energy demands and in preventing further CO_2 emissions.[1–6] However, this practical application is currently challenged by the low activity and selectivity of the CO_2 reduction reaction (CO_2RR) because of the high kinetic barriers and competition with the hydrogen evolution reaction (HER) in aqueous media.[7–9] Strategies, including exploring novel catalysts[8,9] or using non-aqueous electrolyte such as ionic liquid,[10–12] have been extensively studied to reduce reaction barriers or suppress HER. Highly selective CO_2 reduction requires catalysts to have specific electronic structures that could facilitate the CO_2 activation process and also properly bind reaction intermediates, not too strong or too weak.[13] A representative example is a transition-metal (TM) catalyst such as Au, which has been demonstrated to convert CO_2 to carbon monoxide (CO) with high selectivity,[14–16] whereas Pt, with only one d-band electron less, generates H_2 exclusively and can be easily poisoned by CO.[17,18] Other earth-abundant TMs such as Fe, Co, and Ni are rarely studied as CO_2 to CO catalysts, mainly because of their good HER activities as well as the strong bonding between CO and the metal surfaces.[17–21] Therefore, how to effectively tune the catalytic electronic properties plays a critical role in searching for active CO_2RR catalysts.

The Bigger Picture

Using clean electricity to reduce CO_2 to chemicals or fuels is becoming increasingly important to renewable energy applications and environmental protection. The challenge comes from the strong competition with the hydrogen evolution reaction in aqueous solutions, especially for those earth-abundant transition metals such as Ni, which dramatically lowers the CO_2 reduction selectivity. Isolating the transition-metal single atoms into a graphene matrix can significantly tune their catalytic behaviors to favor the CO_2-to-CO reduction pathway, reaching a high CO selectivity of more than 90%. This work creates an important platform in designing active and low-cost CO_2 reduction catalysts with high selectivity toward fuels, opening up great opportunities for both technological applications in renewable energies and fundamental mechanism studies in catalysis.

Please cite this article in press as: Jiang et al., Transition-Metal Single Atoms in a Graphene Shell as Active Centers for Highly Efficient Artificial Photosynthesis, Chem (2017), https://doi.org/10.1016/j.chempr.2017.09.014

Different methods, such as metal oxidation and metal alloying, have been demonstrated to be successful in engineering TM electronic states for improved CO_2RR activities.[7,8,16,22–24] However, these engineering processes on TM catalysts usually result in complicated atomic structures and coordination, making it difficult to study and understand the possible catalytic active sites. Instead, introducing TM atoms into a well-established material matrix could open up great opportunities to (1) tune the electronic properties of TMs as CO_2RR active sites and (2) at the same time maintain relatively simple atomic coordination for fundamental mechanism studies.[9,25] In addition, those TM atoms trapped in a confined environment cannot be easily moved around during catalysis, which prevents the nucleation or reconstructions of surface atoms observed in many cases.[26–29] Graphene layers are of particular interest as host for TM atoms because of their high electron conductivity, chemical stability, and inertness to both CO_2 reduction and HER catalytic reactions.[30] TM atoms can be trapped in the naturally or chemically formed defects of the graphene such as single vacancies (SVs) and double vacancies (DVs), presenting distinctively different properties from bulk metal materials.[31–33] The introduction of N dopants can generate graphene defects that could significantly increase the concentration of TM atoms coordinated within the layers.[34] Although some previous studies suggested CO_2-to-CO catalysis on M-N-C sites, there was no direct evidence to demonstrate the single-atom morphology or the coordination environment of the active sites.[35,36] Here, we report graphene shells (GSs) with Ni atoms embedded as a highly active electrocatalyst for CO_2 reduction to CO in an aqueous electrolyte. We employed three-dimensional (3D) atom probe tomography (APT) to directly identify the single Ni atomic sites in graphene vacancies. With density functional theory (DFT) calculations, we show that, compared with metallic Ni, Ni atomic sites in graphene can dramatically lower the CO_2 activation barrier, weaken the binding with CO for facile product release, and suppress the proton reduction side reaction. As a result, the catalyst exhibits a high faradic efficiency (FE) of ~93.2% toward CO formation under a significant current of ~20 mA/mg, which represents a turnover frequency (TOF) of ~8 s^{-1} for the active Ni center, and can be further improved with a gas diffusion layer electrode in a flow cell.

RESULTS

The catalysts were synthesized by electrospinning of polymer nanofibers (NFs) with Ni and N precursors homogeneously distributed (Supplemental Experimental Procedures). Graphitized carbon NFs (CNFs, ~200 nm in diameter) catalyzed by uniformly dispersed Ni nanoparticles (NPs) (~20 nm in diameter) were obtained after the carbonization process of polymers (Figures 1A and 1B).[37–39] Carbon atoms alloyed with Ni under high temperature precipitated out and were catalyzed to form graphene layers on the Ni metal surface during the cooling down process. A closer observation of the Ni NPs by aberration-corrected scanning transmission electron microscopy (STEM) in Figure 1C reveals that the NP is tightly encapsulated by a few layers (~10 nm) of graphene, as confirmed by the averaged layer spacing of ~0.34 nm (NiN-GS; Figure S1). No Ni clusters were observed within the GS. This shell prevents the Ni NP from direct contact with the aqueous electrolyte and can thus dramatically suppress HER. The existence of Ni atoms in the surface shell was confirmed by energy-dispersive X-ray spectroscopy (EDS) mapping in Figure 1D (Figure S2 and Supplemental Experimental Procedures). The Z-contrast STEM image on the left shows three bright areas representing three Ni NPs, with one of them highlighted by the yellow circle. In the Ni mapping image (marked by green dots), in addition to the NP regions with concentrated signals, Ni peaks were also detected in the neighboring carbon areas (Figure S2), demonstrating the successful incorporation of Ni atoms in the GS. N doping here plays a critical role in

[1]Rowland Institute, Harvard University, Cambridge, MA 02142, USA

[2]SUNCAT Center for Interface Science and Catalysis, Department of Chemical Engineering, Stanford University, Stanford, CA 94305, USA

[3]Center for Nanoscale Systems, Harvard University, Cambridge, MA, USA

[4]Department of Materials Science and Engineering, Stanford University, Stanford, CA 94305, USA

[5]Department of Chemistry and Chemical Biology, Harvard University, Cambridge, MA 02138, USA

[6]Canadian Light Source Inc., University of Saskatchewan, 44 Innovation Boulevard, Saskatoon, SK S7N 2V3, Canada

[7]Shanghai Key Laboratory of Molecular Catalysis and Innovative Materials, Collaborative Innovation Center of Chemistry for Energy Materials, Department of Chemistry, Fudan University, Shanghai 200433, China

[8]School of Engineering and Applied Sciences, Harvard University, Cambridge, MA 02142, USA

[9]SUNCAT Center for Interface Science and Catalysis, SLAC National Accelerator Laboratory, 2575 Sand Hill Road, Menlo Park, CA 94025, USA

[10]Stanford Institute for Materials and Energy Sciences, SLAC National Accelerator Laboratory, 2575 Sand Hill Road, Menlo Park, CA 94025, USA

[11]These authors contributed equally

[12]Lead Contact

*Correspondence: hwang@rowland.harvard.edu

https://doi.org/10.1016/j.chempr.2017.09.014

Please cite this article in press as: Jiang et al., Transition-Metal Single Atoms in a Graphene Shell as Active Centers for Highly Efficient Artificial Photosynthesis, Chem (2017), https://doi.org/10.1016/j.chempr.2017.09.014

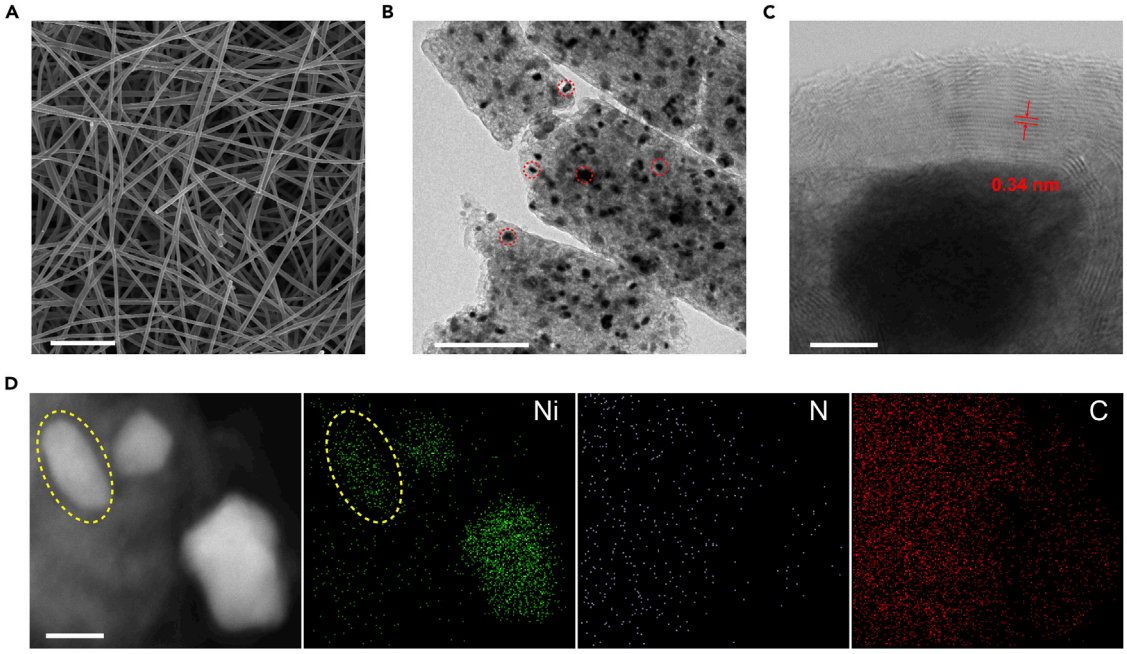

Figure 1. Characterizations of NiN-GS Catalysts

(A) Scanning electron microscopy (SEM) image of carbonized electrospun polymer NFs. Scale bar, 5 μm.

(B) TEM image of a ball-milled NiN-GS catalyst. The dark dots (highlighted by red circles as examples) uniformly distributed in the CNF are Ni NPs. Scale bar, 200 nm.

(C) Aberration-corrected STEM image of a Ni NP tightly wrapped by a few graphene layers. The Ni NP is ~20 nm in diameter. The GS is ~10 nm thick. The layer spacing is measured to be 0.34 nm. Scale bar, 5 nm.

(D) EDS mapping of the NiN-GS catalyst. Three Ni NPs were observed in the STEM image on the left, which is consistent with the Ni mapping image, with one of the NPs indicated by the yellow circle. Ni signals were detected in areas away from the NPs, demonstrating the successful incorporation of Ni atoms in graphene layers. The selected area spectra are shown in Figures S2 and S5. Scale bar, 20 nm.

creating defects in the graphene layers, which helps to trap and bond a significant number of Ni atoms in the GS.[34] This is demonstrated by both Raman and transmission electron microscopy (TEM) characterizations where the graphene layers in NiN-GS present a defective nature compared with the sample without N incorporation (Ni-GS; Figures S3 and S4 and Supplemental Experimental Procedures).[40] In addition, no Ni signals were detected in the GS outside the Ni NP in Ni-GS, because of the high quality of graphene synthesized (Figure S5). Those coordinated Ni atoms within the graphene layers in NiN-GS showed distinctively different oxidation states from Ni NPs covered below by X-ray photoelectron spectroscopy (XPS; Figure S6), suggesting the successful tuning of Ni electronic structures and thus the possible tuning of its catalytic activities.

The electrocatalytic CO_2RR performance of the NiN-GS catalyst, drop casted on a glassy carbon current collector, was performed in 0.1 M potassium bicarbonate ($KHCO_3$) electrolyte in a customized H cell (Supplemental Experimental Procedures). The different cyclic voltammograms (CVs) in CO_2 and N_2 saturated electrolyte suggest that reactions other than HER occur when CO_2 is present (Figures 2A and S7). Gas products were analyzed by gas chromatography (GC) at potential steps of 100 mV and further zoomed into 50 mV around the FE peak (Figures 2B and S8 and Supplemental Experimental Procedures). Detectable CO signals start at –0.35 V versus reversible hydrogen electrode (RHE), suggesting the onset overpotential of CO_2 to CO to be less than 230 mV (Figure S9). As the potential goes more negative, the FE of CO increases as the HER decreases (Figure 2B). The overall FE under different potentials ranges from 91.2% to 105.8% (Figures 2B, Table S1).

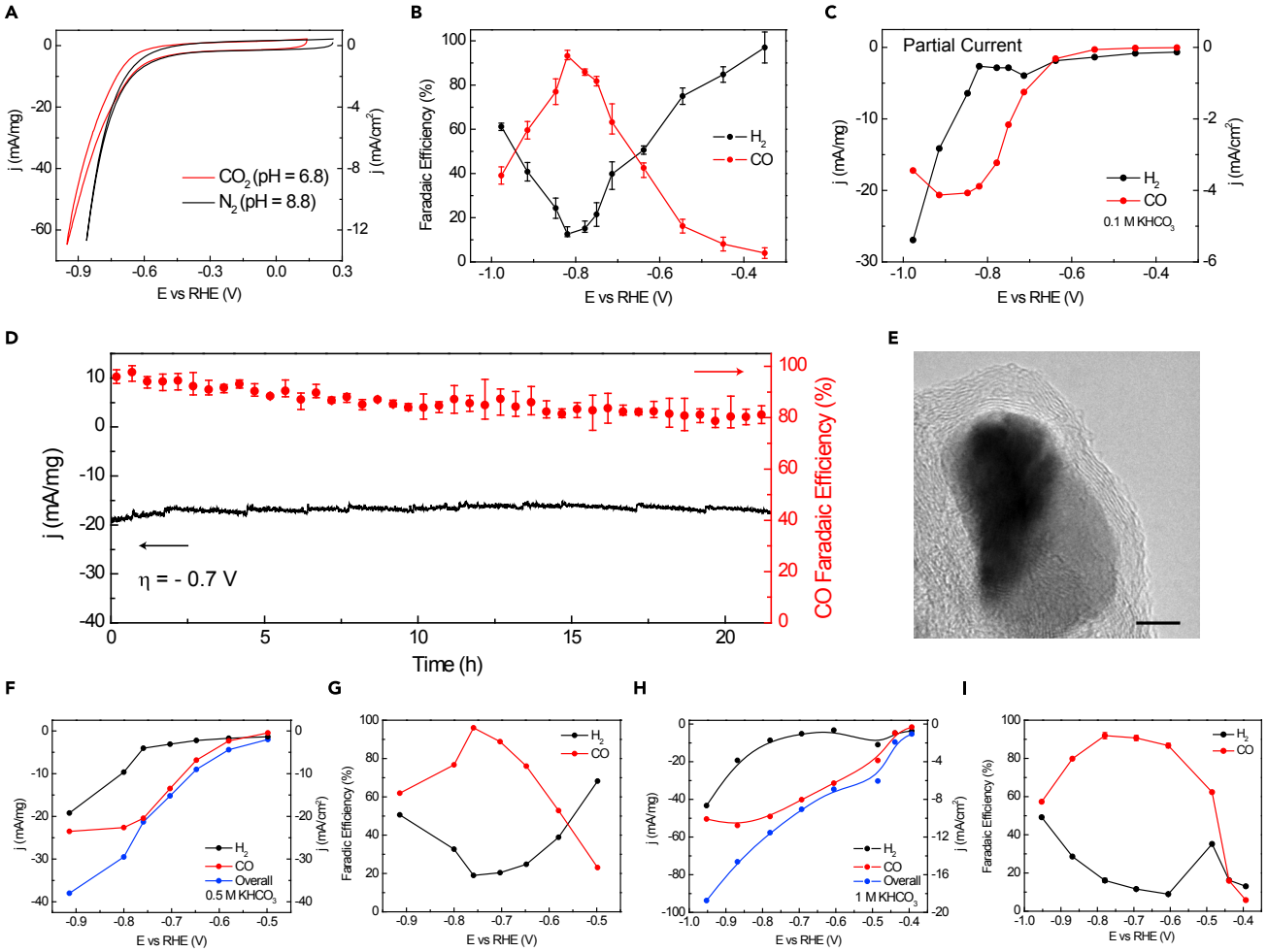

Figure 2. Electrocatalytic CO_2 Reduction Performance of NiN-GS

(A) CVs of NiN-GS in CO_2 and N_2 saturated electrolyte, suggesting a different reaction pathway when CO_2 is present.

(B) FEs of H_2 and CO under different applied potentials for NiN-GS. The error bars are based on three identical samples. The highest CO FE is 93.2% under –0.82 V versus RHE, with an overpotential of –0.7 V. The error bars represent three identical samples.

(C) Partial currents of H_2 and CO. The CO evolution current density is around 20 mA/mg under the highest CO FE.

(D) Long-term electrolysis test under –0.7 V overpotential. The high FE of CO is maintained for more than 20 hr, suggesting good stability of the NiN-GS catalyst. The error bars represent three identical samples.

(E) The TEM image of post-catalysis NiN-GS. Scale bar, 5 nm.

(F and G) CO_2RR catalytic performance (current densities in F and FEs in G) of 1 mg/cm^2 NiN-GS catalyst on a high-surface-area CFP electrode in 0.5 M $KHCO_3$ electrolyte.

(H and I) CO_2RR performance (current densities in H and FEs in I) of NiN-GS catalyst on a gas diffusion layer electrode in a flow cell configuration. The catalyst mass loading is the same as for glassy carbon electrode in (A)–(D).

The highest FE of CO_2 to CO reaches 93.2% at 0.7 V overpotential, with a CO evolution current density of ~20 mA/mg (4 mA/cm^2 at 0.2 mg/cm^2 mass loading; Figures 2C and S10). An isotope $^{13}CO_2$ labeling experiment was performed on GC-mass spectroscopy to confirm that the gas product of CO comes from CO_2 reduction (Figure S11 and Supplemental Experimental Procedures). The Tafel slope plotted with electrolysis currents and overpotentials was 138.5 mV/decade (Figure S12).[9,40–42] No other gas or liquid products were detected by GC or ^{1}H NMR (Figure S13). Whether these surrounded GSs will be stable under long-term operations is a concern, because if the protection layer breaks, the Ni NPs will be exposed to water and could produce H_2 heavily.[19] Around 80% FE of CO was

Please cite this article in press as: Jiang et al., Transition-Metal Single Atoms in a Graphene Shell as Active Centers for Highly Efficient Artificial Photosynthesis, Chem (2017), https://doi.org/10.1016/j.chempr.2017.09.014

still maintained after more than 20 hr of continuous electrolysis under 0.7 V overpotential (Figure 2D), suggesting the excellent stability of the catalytic sites. A post-catalysis TEM examination also confirmed that the core-shell structure remains intact to prevent contact between Ni NPs and water (Figures 2E and S14). The CO_2RR geometrical current density can be significantly improved to more than 20 mA/cm^2 by loading more NiN-GS catalysts onto high-surface-area carbon fiber paper (CFP) substrate while maintaining high CO FEs in 0.5 M $KHCO_3$ electrolyte (Figures 2F and 2G). In addition, the overpotential can be further improved by applying NiN-GS catalyst (0.2 mg/cm^2) onto a gas diffusion layer electrode in a flow cell (Figures 2H and 2I),[43] where a CO partial current of 31.4 mA/mg was obtained at 0.48 V overpotential (Supplemental Experimental Procedures, Figure S15, and Tables S1 and S2).

Control experiments were performed to provide important clues on the possible active sites in NiN-GS for this highly selective CO_2 reduction. First, it is unlikely that the Ni NP cores are in contact with the electrolyte to participate in the gas reduction reactions. This is confirmed by the TEM images of NiN-GS after an acid leaching process (AL-NiN-GS; Figure S16 and Supplemental Experimental Procedures),[44] which show the Ni NPs to be well protected from concentrated protons by the tightly surrounded GSs. Only by violent ball milling followed by acid leaching can we break off some core-shell structures and allow acids to attack Ni NPs (VAL-NiN-GS; Figure S16 and Supplemental Experimental Procedures). In addition, Ni-GS with Ni NPs embedded presents nearly no activity toward CO formation (Figures S17 and S18). Second, the dramatically decreased CO evolution activity per electrochemical surface area (Figure S19) after acid leaching processes suggest that Ni atoms in the surface GS play a more important role than the N dopants (Figure S20).[36,40,41] Third, Co and Fe catalysts with the same core-shell structure and N doping (Figure S21 and Supplemental Experimental Procedures), however, present lower activity and selectivity toward CO formation than NiN-GS (Figure S22), indicating that the high CO FE is related to the specific electronic structure of Ni sites in the GS.

More detailed characterizations to elucidate the nature of Ni atomic sites in graphene layers become important for a clear understanding of the catalytic active sites. Here, we used APT technology (Figure S23) to reveal[45,46] whether the Ni atoms are isolated single atoms or small clusters and whether the Ni atomic sites are coordinated with N or not. The 3D tomography of NiN-GS catalyst is presented in Movie S1, and the projected 2D image is shown in Figure 3A. Each pixel represents one single atom. As shown in Figure 3B and Movie S2, away from the areas with concentrated Ni (Ni NPs), there are also a significant number of Ni atoms dispersed in carbon, consistent with our EDX mapping in Figure 1D. The contour map with an interval of 2 at % in Figure 3C provides detailed distribution information on Ni atoms in the catalyst, with decreased Ni atom concentrations away from the Ni sources. The local coordination environment of the Ni atoms is shown by taking a closer look at the graphene layers in Figure 3D. There are a few Ni single atoms coordinated in graphene vacancies, providing direct evidence of the single Ni atomic site. No Ni clusters were observed. In addition, we also noticed that there is one Ni atom coordinated with one N atom in a graphene vacancy, suggesting a small ratio of Ni atomic sites coordinated with N atoms. More detailed information about the surrounding coordination of Ni atomic sites can be extracted from statistics and quantitative analysis (Figure 3F). The selected area with dispersed Ni atoms is indicated by the yellow circle in Figure 3A and enlarged in Figure 3E. Among all the Ni atoms in this area, 83% are single atoms, without neighboring Ni atoms closer than 2.2 Å (Figure S24). In addition, in those Ni single atoms, only 0.2% of them are directly coordinated with one neighboring N (less than 2 Å), suggesting that most of the Ni atomic sites are coordinated with C atoms. Single-atom

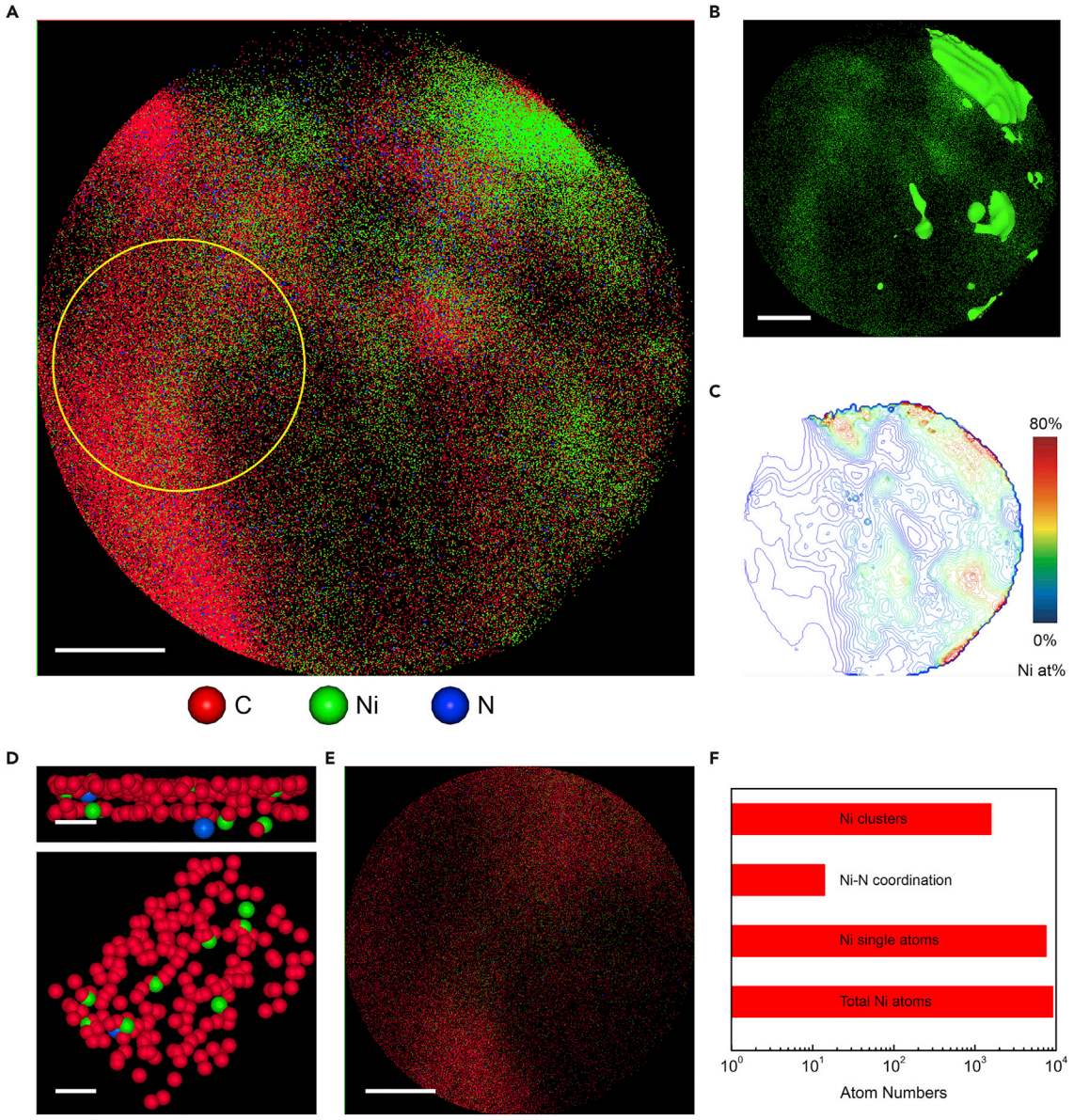

Figure 3. ATP of the NiN-GS Catalyst

(A) The 2D atom map of NiN-GS. The yellow circle represents the selected area for statistical studies in (E) and (F). Scale bar, 10 nm.

(B) The 2D projected view of Ni atoms. The green areas represent Ni-rich areas (>50 at %). Away from the Ni sources, there are still a significant number of Ni atoms dispersed in the carbon area. Scale bar, 10 nm.

(C) The contour map of Ni concentration with an interval of 2 at %.

(D) Zoomed in side view (upper) and top view (lower) of graphene layers with Ni single atoms coordinated in vacancies. Only one Ni atom is directly coordinated with one N atom. Scale bars, 1 nm.

(E) Atom map of the selected area in (A) as indicated by the yellow circle. Scale bar, 5 nm.

(F) The statistics of the selected area in (E). Most of the Ni atoms are in single-atom morphology, and 0.2% of them are coordinated with N atoms.

coordination in the graphene shell is also observed by X-ray absorption spectroscopy as the small peak at ~1.4 Å in R space beside the dominating Ni–Ni bonding signal from those embedded Ni NPs (Supplemental Experimental Procedures and Figure S24). In addition, the *in situ* electrochemical attenuated total reflection infrared spectroscopy (ATR-IR) result with adsorbed monolayer CO as a surface probe further demonstrates the single Ni atomic sites on the surface of the NiN-GS catalyst

Please cite this article in press as: Jiang et al., Transition-Metal Single Atoms in a Graphene Shell as Active Centers for Highly Efficient Artificial Photosynthesis, Chem (2017), https://doi.org/10.1016/j.chempr.2017.09.014

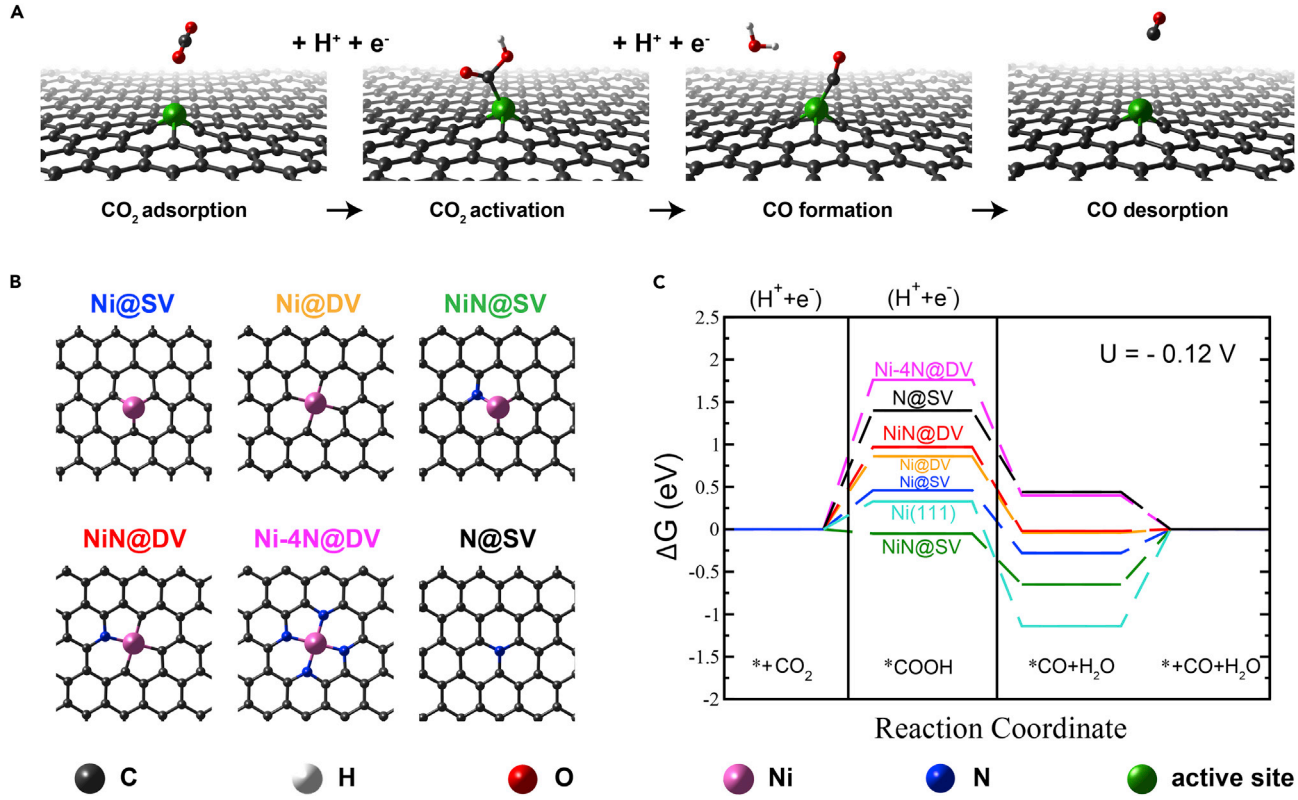

Figure 4. Simulations of CO_2-to-CO Reduction on Different Atomic Sites

(A) Schematic of the reaction steps of electrocatalytic CO_2 to CO reduction.

(B) Different atomic configurations in graphene for the DFT calculations.

(C) The free energy diagram of CO_2 to CO conversion on different atomic sites under an equilibrium potential of –0.12 V versus RHE.

(Figure S25).[24,47] Therefore, we believe that the Ni sites in GS should be the active centers for electrocatalytic CO_2 to CO conversion, which exhibits a high TOF of ~8 s^{-1} and a cumulative turnover number (TON) of up to 454,000 under –0.7 V overpotential during 20 hr of continuous electrolysis (Figure S26 and Supplemental Experimental Procedures).

DISCUSSION

To further investigate the origin of the activity of the NiN-GS catalyst, we studied the reaction steps involved in the CO_2 to CO electrocatalytic reduction by using DFT calculations (Figure 4A). We considered Ni atoms trapped in single or double vacancies (Ni@SV and Ni@DV, respectively) of the graphene sheet, with a variety of possible N coordination to Ni sites as well as N dopants (N@SV) (Figure S27 and Supplemental Experimental Procedures), among which the most stable and active structures are shown in Figure 4B (Table S3). A simple thermochemical analysis shows that the pathway for CO_2 reduction to CO goes through *COOH and *CO intermediates (Figures 4A).[48–50] The solvation correction is included in Figure S28 (Supplemental Experimental Procedures). The free energy diagram for each reaction step on different atomic structures, including the Ni (111) surface, was calculated at the equilibrium potential (−0.12 V versus RHE) in Figure 4C, where CO_2 activation (*COOH formation) or CO desorption are suggested to be the rate-limiting steps on different sites. As an example, on Ni (111) metal surface, even though the *COOH formation is facile, the binding with CO is too strong as indicated by the deep thermodynamic sink

(−1.14 eV) in Figure 4C, which dramatically limits the CO desorption process and thus the overall catalytic performance. This is consistent with the observation that Ni metal evolves primarily H_2 under CO_2 reduction conditions.[18] However, when Ni atoms are coordinated in graphene layers, the electronic structure is drastically changed, exhibiting a much higher projected density of states around Fermi energy than that of Ni (111) (Figures S6 and S29). As a result, the binding with CO is significantly weakened for a facile CO desorption (Figure 4C and Table S4). In addition, compared with N dopants in graphene, the Ni atomic sites such as Ni@SV and NiN@SV present decreased *COOH formation energies (Figure 4C and Table S4).[21] Direct coordination of N to Ni atoms in graphene layers helps to pull the electrons away from Ni, which as a result makes the *COOH formation thermodynamically downhill on NiN@SV. However, it binds CO slightly more strongly than Ni@SV (Table S4). Combined with APT characterizations, this analysis therefore suggests that the Ni atoms coordinated in the graphene vacancies, such as Ni@SV and Ni@DV, are the major active sites for electrocatalytic CO_2 reduction to CO, where N atoms play a critical role in generating defects in graphene to trap Ni atoms. The minority atomic sites in this catalyst system, such as NiN@SV or NiN@DV, could also be highly active for CO_2RR as suggested by the DFT simulations. The calculated H-binding energy, a good descriptor for HER activity,[51–53] suggests significantly suppressed hydrogen generation on Ni@SV, Ni@DV, and NiN@SV sites (ΔG_H = 0.50, 0.56, and 0.52 eV, respectively) in comparison with Ni (111) metal surface (ΔG_H = −0.26 eV),[52,53] which is consistent with our experimental results (Table S5). The CO_2RR selectivity of different active sites can be further evaluated by the difference between the thermodynamic limiting potentials for CO_2 reduction and HER, $U_L(CO_2) - U_L(H_2)$, which confirms the high selectivity of both Ni@SV and Ni@DV (Figure S30). Because of the different electronic structures, Co atomic sites present stronger CO binding and higher HER catalytic activity than Ni sites (Table S6), which explains its lower CO selectivity (Figure S22).

For a practical electrosynthetic cell of CO_2 reduction to fuels, an active and stable oxygen evolution reaction (OER) catalyst needs to be paired to efficiently oxidize water and free the protons.[10,54] Different from previous literature where CO_2RR and OER catalysts were usually separated by a bipolar membrane and operated in different pH solutions,[55,56] here we developed the Li^+-tuned Co_3O_4 NPs as an active and stable OER catalyst in neutral pH to be coupled with NiN-GS for a pH-equal (pH 7.5) electrolysis system (Figures S31–S35 and Supplemental Experimental Procedures).[20] Powered by a single cell of commercialized $GaInP_2$/GaAs/Ge TJ photovoltaic, our artificial photosynthesis system delivers a peak solar-to-CO efficiency of 12.7% (Figures S36 and S37). Incorporating TM atoms into a well-defined 2D matrix can effectively tune their electronic structures and thus favor the desired reaction pathways. Given the wide variety of 2D layered materials, which provide different types of chemical environments for tuning different TM atoms, this approach creates an important platform for designing active CO_2 reduction catalysts with high selectivity toward CO and higher-value hydrocarbons, which is of great importance to both technological applications in renewable energies and fundamental mechanism studies in catalysis.

EXPERIMENTAL PROCEDURES

The NiN-GS catalyst was first prepared by electrospinning a precursor solution containing polyacrylonitrile (M_w = 150,000), polypyrrolidone (M_w = 1,300,000), $Ni(NO_3)_2$ $6H_2O$, dicyandiamide, and dimethylformamide, followed by a polymer nanofiber oxidation and a carbonization procedure (Supplemental Experimental Procedures). The as-synthesized NiN-GS catalyst was ball milled for 5 min to nanopowder for catalysis and characterization.

The STEM characterization in Figure 1C and other EDS analysis were carried out with a JEOL ARM200F aberration-corrected scanning transmission electron microscope. All other TEM images were obtained with a JEOL 2100 TEM. Specimens for 3D APT were prepared with an FEI Helios 660 Nanolab Dual-Beam FIB/SEM. APT was then performed with a Cameca LEAP 4000 HR operated in laser mode. Approximately 2.3 million atoms were collected in the dataset presented. The data were reconstructed and analyzed with Cameca's IVAS software according to standard reconstruction protocols.

In situ electrochemical ATR-IR measurements were run on a catalyst layer covered hemicylindrical Si prism with a Nicolet IS50 FTIR spectrometer. Raman spectroscopy was carried out on a WITEC CRM200 confocal Raman spectrometer with a 532 nm laser source. XPS was obtained with a Thermo Scientific K-Alpha ESCA spectrometer, and the surface componential content and peak fitting was analyzed with the Thermo Avantage V5 program for selected elemental scans. The Ni K-edge XAS was acquired in fluorescence mode with the SXRMB beamline of Canadian Light Source. Powder XRD data were collected with a Bruker D2 Phaser diffractometer.

The electrochemical measurements were run at 25°C in a customized gas-tight H cell (Figure S8) or flow cell (Figure S15) or a 3D-printed electrosynthetic cell (Figure S35) separated by Nafion 117 membrane. A BioLogic VMP3 workstation was used to record the electrochemical response. All measured potentials in this work were converted to the RHE scale with manual *iR* compensation. During electrolysis, CO_2 gas was delivered into the cathodic compartment containing CO_2-saturated $KHCO_3$ electrolyte and vented into a Shimadzu GC-2014 gas chromatograph equipped with a thermal conductivity detector and a flame ionization detector coupled with a methanizer.

All other experimental and setup details, as well the DFT calculations, are provided in the Supplemental Experimental Procedures.

SUPPLEMENTAL INFORMATION

Supplemental Information includes Supplemental Experimental Procedures, 37 figures, 6 tables, and 2 movies and can be found with this article online at https://doi.org/10.1016/j.chempr.2017.09.014.

AUTHOR CONTRIBUTIONS

H.W. conceived the project. H.W. and K.J. synthesized materials and measured catalysts. H.W., K.J., A.J.A., Y.L., Z.L., J.L., Y.H., and Y.Z. characterized materials. S.S., K.C., and J.K.N. performed simulations. All authors analyzed the results. H.W., K.J., and S.S. wrote the manuscript. H.W. supervised the project.

ACKNOWLEDGMENTS

This work was supported by the Rowland Fellows Program at the Rowland Institute of Harvard University. H.W. and K.J. acknowledge great support from the Friend group at Harvard University. S.S., Y.L., Z.L., J.K.N., and Y.C. acknowledge support from the Global Climate and Energy Project at Stanford University. K.C. and J.K.N. acknowledge support from the Joint Center for Artificial Photosynthesis, a DOE Energy Innovation Hub, supported through the Office of Science of the US Department of Energy under award number DESC0004993. W.B.C. and Y.Z. acknowledge support from the 973 Program of the Chinese Ministry of Science and Technology (2015CB932303) and Natural Science Foundation of China (21733004 and 21327901). This work was performed in part at the Center for Nanoscale Systems

(CNS), a member of the National Nanotechnology Infrastructure Network, which is supported by the National Science Foundation under award no. ECS-0335765. The CNS is part of Harvard University. We acknowledge great support from Spectrolab for the triple-junction solar cell used in this work. We acknowledge the Nocera group at Harvard University for helping with the solar simulator. We acknowledge the helpful discussion on flow cells with Prof. Kenis and Mr. Sumit at the University of Illinois at Urbana-Champaign.

Received: August 1, 2017
Revised: September 15, 2017
Accepted: September 26, 2017
Published: October 19, 2017

REFERENCES AND NOTES

1. Cook, T.R., Dogutan, D.K., Reece, S.Y., Surendranath, Y., Teets, T.S., and Nocera, D.G. (2010). Solar energy supply and storage for the legacy and nonlegacy worlds. Chem. Rev. *110*, 6474–6502.

2. Meyer, T.J. (1989). Chemical approaches to artificial photosynthesis. Acc. Chem. Res. *22*, 163–170.

3. Sakimoto, K.K., Wong, A.B., and Yang, P. (2016). Self-photosensitization of nonphotosynthetic bacteria for solar-to-chemical production. Science *351*, 74–77.

4. Liu, C., Colón, B.C., Ziesack, M., Silver, P.A., and Nocera, D.G. (2016). Water splitting–biosynthetic system with CO2 reduction efficiencies exceeding photosynthesis. Science *352*, 1210–1213.

5. Lewis, N.S., and Nocera, D.G. (2006). Powering the planet: chemical challenges in solar energy utilization. Proc. Natl. Acad. Sci. USA *103*, 15729–15735.

6. Jhong, H.-R.M., Ma, S., and Kenis, P.J.A. (2013). Electrochemical conversion of CO2 to useful chemicals: current status, remaining challenges, and future opportunities. Curr. Opin. Chem. Eng. *2*, 191–199.

7. Li, C.W., Ciston, J., and Kanan, M.W. (2014). Electroreduction of carbon monoxide to liquid fuel on oxide-derived nanocrystalline copper. Nature *508*, 504–507.

8. Gao, S., Lin, Y., Jiao, X., Sun, Y., Luo, Q., Zhang, W., Li, D., Yang, J., and Xie, Y. (2016). Partially oxidized atomic cobalt layers for carbon dioxide electroreduction to liquid fuel. Nature *529*, 68–71.

9. Lin, S., Diercks, C.S., Zhang, Y.-B., Kornienko, N., Nichols, E.M., Zhao, Y., Paris, A.R., Kim, D., Yang, P., Yaghi, O.M., et al. (2015). Covalent organic frameworks comprising cobalt porphyrins for catalytic CO2 reduction in water. Science *349*, 1208–1213.

10. Asadi, M., Kim, K., Liu, C., Addepalli, A.V., Abbasi, P., Yasaei, P., Phillips, P., Behranginia, A., Cerrato, J.M., Haasch, R., et al. (2016). Nanostructured transition metal dichalcogenide electrocatalysts for CO2 reduction in ionic liquid. Science *353*, 467–470.

11. Rosen, B.A., Salehi-Khojin, A., Thorson, M.R., Zhu, W., Whipple, D.T., Kenis, P.J.A., and Masel, R.I. (2011). Ionic liquid–mediated selective conversion of CO2 to CO at low overpotentials. Science *334*, 643–644.

12. Costentin, C., Robert, M., and Savéant, J.-M. (2013). Catalysis of the electrochemical reduction of carbon dioxide. Chem. Soc. Rev. *42*, 2423–2436.

13. Bligaard, T., Nørskov, J.K., Dahl, S., Matthiesen, J., Christensen, C.H., and Sehested, J. (2004). The Brønsted–Evans–Polanyi relation and the volcano curve in heterogeneous catalysis. J. Catal. *224*, 206–217.

14. Zhu, W., Michalsky, R., Metin, Ö., Lv, H., Guo, S., Wright, C.J., Sun, X., Peterson, A.A., and Sun, S. (2013). Monodisperse Au nanoparticles for selective electrocatalytic reduction of CO2 to CO. J. Am. Chem. Soc. *135*, 16833–16836.

15. Liu, M., Pang, Y., Zhang, B., De Luna, P., Voznyy, O., Xu, J., Zheng, X., Dinh, C.T., Fan, F., Cao, C., et al. (2016). Enhanced electrocatalytic CO2 reduction via field-induced reagent concentration. Nature *537*, 382–386.

16. Chen, Y., Li, C.W., and Kanan, M.W. (2012). Aqueous CO2 reduction at very Low overpotential on oxide-derived Au nanoparticles. J. Am. Chem. Soc. *134*, 19969–19972.

17. Kuhl, K.P., Hatsukade, T., Cave, E.R., Abram, D.N., Kibsgaard, J., and Jaramillo, T.F. (2014). Electrocatalytic conversion of carbon dioxide to methane and methanol on transition metal surfaces. J. Am. Chem. Soc. *136*, 14107–14113.

18. Hori, Y., Wakebe, H., Tsukamoto, T., and Koga, O. (1994). Electrocatalytic process of CO selectivity in electrochemical reduction of CO2 at metal electrodes in aqueous media. Electrochim. Acta *39*, 1833–1839.

19. Gong, M., Zhou, W., Tsai, M.-C., Zhou, J., Guan, M., Lin, M.-C., Zhang, B., Hu, Y., Wang, D.-Y., Yang, J., et al. (2014). Nanoscale nickel oxide/nickel heterostructures for active hydrogen evolution electrocatalysis. Nat. Commun. *5*, 4695.

20. Wang, H., Lee, H.-W., Deng, Y., Lu, Z., Hsu, P.-C., Liu, Y., Lin, D., and Cui, Y. (2015). Bifunctional non-noble metal oxide nanoparticle electrocatalysts through lithium-induced conversion for overall water splitting. Nat. Commun. *6*, 7261.

21. Shi, C., Hansen, H.A., Lausche, A.C., and Norskov, J.K. (2014). Trends in electrochemical CO2 reduction activity for open and close-packed metal surfaces. Phys. Chem. Chem. Phys. *16*, 4720–4727.

22. Chen, Y., and Kanan, M.W. (2012). Tin oxide dependence of the CO2 reduction efficiency on tin electrodes and enhanced activity for tin/tin oxide thin-film catalysts. J. Am. Chem. Soc. *134*, 1986–1989.

23. Kim, D., Resasco, J., Yu, Y., Asiri, A.M., and Yang, P. (2014). Synergistic geometric and electronic effects for electrochemical reduction of carbon dioxide using gold–copper bimetallic nanoparticles. Nat. Commun. *5*, 4948.

24. Jiang, K., Wang, H., Cai, W.-B., and Wang, H. (2017). Li electrochemical tuning of metal oxide for highly selective CO2 reduction. ACS Nano *11*, 6451–6458.

25. Nishihara, H., Hirota, T., Matsuura, K., Ohwada, M., Hoshino, N., Akutagawa, T., Higuchi, T., Jinnai, H., Koseki, Y., Kasai, H., et al. (2017). Synthesis of ordered carbonaceous frameworks from organic crystals. Nat. Commun. *8*, 109.

26. Manthiram, K., Beberwyck, B.J., and Alivisatos, A.P. (2014). Enhanced electrochemical methanation of carbon dioxide with a dispersible nanoscale copper catalyst. J. Am. Chem. Soc. *136*, 13319–13325.

27. Lei, F., Liu, W., Sun, Y., Xu, J., Liu, K., Liang, L., Yao, T., Pan, B., Wei, S., and Xie, Y. (2016). Metallic tin quantum sheets confined in graphene toward high-efficiency carbon dioxide electroreduction. Nat. Commun. *7*, 12697.

28. Yang, M., Li, S., Wang, Y., Herron, J.A., Xu, Y., Allard, L.F., Lee, S., Huang, J., Mavrikakis, M., and Flytzani-Stephanopoulos, M. (2014). Catalytically active Au-O(OH)x- species stabilized by alkali ions on zeolites and mesoporous oxides. Science *346*, 1498–1501.

29. Manthiram, K., Surendranath, Y., and Alivisatos, A.P. (2014). Dendritic assembly of gold nanoparticles during fuel-forming electrocatalysis. J. Am. Chem. Soc. *136*, 7237–7240.

30. Novoselov, K.S., Geim, A.K., Morozov, S.V., Jiang, D., Zhang, Y., Dubonos, S.V., Grigorieva,

I.V., and Firsov, A.A. (2004). Electric field effect in atomically thin carbon films. Science *306*, 666–669.

31. Rodríguez-Manzo, J.A., Cretu, O., and Banhart, F. (2010). Trapping of metal atoms in vacancies of carbon nanotubes and graphene. ACS Nano *4*, 3422–3428.

32. Giovanni, M., Poh, H.L., Ambrosi, A., Zhao, G., Sofer, Z., Sanek, F., Khezri, B., Webster, R.D., and Pumera, M. (2012). Noble metal (Pd, Ru, Rh, Pt, Au, Ag) doped graphene hybrids for electrocatalysis. Nanoscale *4*, 5002–5008.

33. Krasheninnikov, A.V., Lehtinen, P.O., Foster, A.S., Pyykkö, P., and Nieminen, R.M. (2009). Embedding transition-metal atoms in graphene: structure, bonding, and magnetism. Phys. Rev. Lett. *102*, 126807.

34. Li, Y., Zhou, W., Wang, H., Xie, L., Liang, Y., Wei, F., Idrobo, J.-C., Pennycook, S.J., and Dai, H. (2012). An oxygen reduction electrocatalyst based on carbon nanotube-graphene complexes. Nat. Nanotech. *7*, 394–400.

35. Su, P., Iwase, K., Nakanishi, S., Hashimoto, K., and Kamiya, K. (2016). Nickel-nitrogen-modified graphene: an efficient electrocatalyst for the reduction of carbon dioxide to carbon monoxide. Small *12*, 6083–6089.

36. Varela, A.S., Ranjbar Sahraie, N., Steinberg, J., Ju, W., Oh, H.-S., and Strasser, P. (2015). Metal-doped nitrogenated carbon as an efficient catalyst for direct CO2 electroreduction to CO and hydrocarbons. Angew. Chem. Int. Ed. *54*, 10758–10762.

37. Chen, Z., Ren, W., Gao, L., Liu, B., Pei, S., and Cheng, H.-M. (2011). Three-dimensional flexible and conductive interconnected graphene networks grown by chemical vapour deposition. Nat. Mater. *10*, 424–428.

38. Deng, D., Novoselov, K.S., Fu, Q., Zheng, N., Tian, Z., and Bao, X. (2016). Catalysis with two-dimensional materials and their heterostructures. Nat. Nanotech. *11*, 218–230.

39. Kumar, B., Asadi, M., Pisasale, D., Sinha-Ray, S., Rosen, B.A., Haasch, R., Abiade, J., Yarin, A.L., and Salehi-Khojin, A. (2013). Renewable and metal-free carbon nanofibre catalysts for carbon dioxide reduction. Nat. Commun. *4*, 2819.

40. Sharma, P.P., Wu, J., Yadav, R.M., Liu, M., Wright, C.J., Tiwary, C.S., Yakobson, B.I., Lou, J., Ajayan, P.M., and Zhou, X.-D. (2015). Nitrogen-doped carbon nanotube arrays for high-efficiency electrochemical reduction of CO2: on the understanding of defects, defect density, and selectivity. Angew. Chem. Int. Ed. *54*, 13701–13705.

41. Wu, J., Yadav, R.M., Liu, M., Sharma, P.P., Tiwary, C.S., Ma, L., Zou, X., Zhou, X.-D., Yakobson, B.I., Lou, J., et al. (2015). Achieving highly efficient, selective, and stable CO2 reduction on nitrogen-doped carbon nanotubes. ACS Nano *9*, 5364–5371.

42. Kornienko, N., Zhao, Y., Kley, C.S., Zhu, C., Kim, D., Lin, S., Chang, C.J., Yaghi, O.M., and Yang, P. (2015). Metal–organic frameworks for electrocatalytic reduction of carbon dioxide. J. Am. Chem. Soc. *137*, 14129–14135.

43. Jhong, H.-R.M., Brushett, F.R., and Kenis, P.J.A. (2013). The effects of catalyst layer deposition methodology on electrode performance. Adv. Energy Mater. *3*, 589–599.

44. Zhao, Y., Nakamura, R., Kamiya, K., Nakanishi, S., and Hashimoto, K. (2013). Nitrogen-doped carbon nanomaterials as non-metal electrocatalysts for water oxidation. Nat. Commun. *4*, 2390.

45. Tedsree, K., Li, T., Jones, S., Chan, C.W.A., Yu, K.M.K., Bagot, P.A.J., Marquis, E.A., Smith, G.D.W., and Tsang, S.C.E. (2011). Hydrogen production from formic acid decomposition at room temperature using a Ag-Pd core-shell nanocatalyst. Nat. Nanotech. *6*, 302–307.

46. Kelly, T.F., and Miller, M.K. (2007). Atom probe tomography. Rev. Sci. Instrum. *78*, 031101.

47. Huo, S.-J., Wang, J.-Y., Yao, J.-L., and Cai, W.-B. (2010). Exploring electrosorption at iron electrode with in situ surface-enhanced infrared absorption spectroscopy. Anal. Chem. *82*, 5117–5124.

48. Hansen, H.A., Varley, J.B., Peterson, A.A., and Nørskov, J.K. (2013). Understanding trends in the electrocatalytic activity of metals and enzymes for CO2 reduction to CO. J. Phys. Chem. Lett. *4*, 388–392.

49. Hansen, H.A., Shi, C., Lausche, A.C., Peterson, A.A., and Norskov, J.K. (2016). Bifunctional alloys for the electroreduction of CO2 and CO. Phys. Chem. Chem. Phys. *18*, 9194–9201.

50. Peterson, A.A., and Nørskov, J.K. (2012). Activity descriptors for CO2 electroreduction to methane on transition-metal catalysts. J. Phys. Chem. Lett. *3*, 251–258.

51. Hinnemann, B., Moses, P.G., Bonde, J., Jørgensen, K.P., Nielsen, J.H., Horch, S., Chorkendorff, I., and Nørskov, J.K. (2005). Biomimetic hydrogen evolution: MoS2 nanoparticles as catalyst for hydrogen evolution. J. Am. Chem. Soc. *127*, 5308–5309.

52. Greeley, J., Jaramillo, T.F., Bonde, J., Chorkendorff, I., and Nørskov, J.K. (2006). Computational high-throughput screening of electrocatalytic materials for hydrogen evolution. Nat. Mater. *5*, 909–913.

53. Greeley, J., Nørskov, J.K., Kibler, L.A., El-Aziz, A.M., and Kolb, D.M. (2006). Hydrogen evolution over bimetallic systems: understanding the trends. ChemPhysChem *7*, 1032–1035.

54. Schreier, M., Curvat, L., Giordano, F., Steier, L., Abate, A., Zakeeruddin, S.M., Luo, J., Mayer, M.T., and Grätzel, M. (2015). Efficient photosynthesis of carbon monoxide from CO2 using perovskite photovoltaics. Nat. Commun. *6*, 7326.

55. Schreier, M., Héroguel, F., Steier, L., Ahmad, S., Luterbacher, J.S., Mayer, M.T., Luo, J., and Grätzel, M. (2017). Solar conversion of CO2 to CO using earth-abundant electrocatalysts prepared by atomic layer modification of CuO. Nat. Energy *2*, 17087.

56. Zhou, X., Liu, R., Sun, K., Chen, Y., Verlage, E., Francis, S.A., Lewis, N.S., and Xiang, C. (2016). Solar-driven reduction of 1 atm of CO2 to formate at 10% energy-conversion efficiency by use of a TiO2-protected III–V tandem photoanode in conjunction with a bipolar membrane and a Pd/C Cathode. ACS Energy Lett. *1*, 764–770.

Chem, Volume *3*

Supplemental Information

Transition-Metal Single Atoms in a Graphene Shell as Active Centers for Highly Efficient Artificial Photosynthesis

Kun Jiang, Samira Siahrostami, Austin J. Akey, Yanbin Li, Zhiyi Lu, Judith Lattimer, Yongfeng Hu, Chris Stokes, Mahesh Gangishetty, Guangxu Chen, Yawei Zhou, Winfield Hill, Wen-Bin Cai, David Bell, Karen Chan, Jens K. Nørskov, Yi Cui, and Haotian Wang

Supplemental Methods

Sample preparation

NiN-GS catalyst was prepared by dissolving 0.5 g polyacrylonitrile (PAN, M_w=150,000), 0.5 g polypyrrolidone (PVP, M_w=1,300,000), 0.5 g $Ni(NO_3)_2 \cdot 6H_2O$, and 0.1 g dicyandiamide (DCDA) in 10 ml of dimethylformamide (DMF) under 80 °C with constant stirring. The solution was then electrospun using a conventional electrospinning set-up with the following parameters: 15 kV of static electric voltage, 15 cm of air gap distance, 5 ml solution and 1.2 ml h^{-1} flow rate. A carbon fiber paper (CFP) substrate (8 × 8 cm) was used as the collection substrate with – 4 kV electric voltage. The electronspun polymer nanofibers (NFs) on the CFP was then heated up to 300 °C in 1.5 h in the box furnace, and kept under the temperature for 0.5 h to oxidize the polymers. After the oxidization process, the NFs were self-detached from the carbon paper resulting in the freestanding film. Those NFs were further carbonized and graphitized under forming gas (5 % H_2 in Ar) atmosphere, with 10 min ramping to 300 °C, and 2 h ramping to 750 °C, where it was maintained for another 1 h and followed by the natural cooling down. Considering the starting mass of 0.1 g Ni (in 0.5 g $Ni(NO_3)_2 \cdot 6H_2O$) and a 60 % mass loss of polymers observed during the oxidation and carbonization processes, the overall Ni to C ratio in NiN-GS catalyst should be more than 5 %. The as-synthesized NiN-GS catalyst was then ball milled (5 min, Mixer/Miller 5100) to nano powders for catalysis and characterizations. Co and Fe catalysts were synthesized with the same method. N-CNF was prepared without the addition of metal salts. Ni-GS catalyst was prepared by electrospinning of poly(vinyl alcohol) (PVA, M_W=85,000) and Ni solution without N (1 g of PVA and 0.5 g of $Ni(NO_3)_2 \cdot 6H_2O$ dissolved in 5 ml H_2O and 5 ml Ethanol mixer), followed with the same carbonization process of NiN-GS. The acid leaching was performed by ultra-sonicating the NiN-GS sample in concentrated HCl (37 wt%) solution for 4 h, followed by repeated centrifuging and water rinsing until neutralization. To further remove the embedded Ni NPs, the violent acid leaching process was performed by first of all ball milling the NiN-GS catalysts for 1 h where each 10 min was stopped for remixing the sample in the vial set, and followed with ultra-sonicating the sample in concentrated HCl acid for more than 8 h.

The OER catalyst Co_3O_4 NPs were directly synthesized on CFP electrode (AvCarb MGL270, FuelCellStore) by a previously developed dip-coating method (*16*). The solution of cobalt nitrate was first prepared by dissolving 40 wt% $Co(NO_3)_2 \cdot 6H_2O$ (Sigma-Aldrich) and 4 wt% PVP (*Mw*=360,000, Sigma-Aldrich) into 56 wt% deionized water. Specifically, 2 g of $Co(NO_3)_2 \cdot 6H_2O$ and 0.2 g of PVP were dissolved into 2.8 ml of deionized water. O_2 plasma-treated CFP was then dipped into the

solution and dried in the vacuum. The $Co(NO_3)_2$/CFP was then heated up to 350 °C in 1 h in air and kept there for another 1 h, where the $Co(NO_3)_2$ was decomposed into Co_3O_4 NPs. The mass loading of Co_3O_4 is measured to be ~ 4 mg/cm^2. The as-grown Co_3O_4 on CFP was made into a pouch cell battery with a piece of Li metal and 1.0 M $LiPF_6$ in 1:1 w/w ethylene carbonate/diethyl carbonate (BASF Chemicals) as electrolyte. The galvanostatic cycling current is set at 0.2 mA/cm^2 and cycle between 0.4 and 3 V vs Li^+/Li. The cutoff voltage of the last discharging step is 4.3 V for thoroughly delithiation. The galvanostatic cycled Co_3O_4 on CFP was then washed by ethanol and H_2O for SEM, XRD, and electrocatalytic characterizations. The IrO_2 benchmark catalyst ink was prepared with the same method of NiN-GS and drop casted onto CFP electrode with the same mass loading of Co_3O_4.

Sample characterizations

The STEM characterization in Figure 1c was carried out using a JEOL ARM200F aberration-corrected scanning transmission electron microscope under 80 kV. All other TEM images were obtained by using a JEOL 2100 transmission electron microscope operated under 200 kV. EDS analysis was performed on a JEOL ARM200F at 60kV, using an EDAX Octane Plus windowless detector. Drift correction was applied during acquisition.

Specimens for the 3D Atom Probe Tomography were prepared using an FEI Helios 660 Nanolab Dual-Beam FIB/SEM. Individual NiN-GS nanofibers (diameter ~ 200 nm) were extracted from the as-prepared matt using an Omniprobe 400 micromanipulator, and then attached via FIB-induced Pt deposition to presharpened silicon microtips for APT analysis and their ends cleaned and shaped using FIB milling. APT was performed using a Cameca LEAP 4000 HR operated in laser mode (355 nm laser). APT parameters were: pulse energy 400 pJ, with a frequency of 100 kHz and a detection rate of 0.5%, and a base temperature of 40 K. Approximately 2.3 million atoms were collected in the dataset presented. The data was reconstructed and analyzed using Cameca's IVAS software, following standard reconstruction protocols.

In situ electrochemical ATR-IR measurement was performed on a NiN-GS catalyst layer or an electrodeposited Ni film-covered Au film on a hemicylindrical Si prism using Nicolet IS50 FTIR spectrometer equipped with a liquid nitrogen cooled MCT-A detector at a bottom-up incidence angle of ca. 65°.[1-2] All spectra were collected at a resolution of 2 cm^{-1} with non-polarized IR radiation, and each single-beam spectrum was an average of 128 scans. An Au foil was used as counter electrode, and a SCE as the reference

electrode. For CO adsorption, the working electrode began with bubbling CO (>99.9% purity) in 0.1 M $NaClO_4$ solution for 20 min at 0.0 V vs. RHE. Then, the dissolved CO was removed from the electrolyte by bubbling Ar for 40 min while maintaining the same electrode potential.

Raman spectroscopy was carried out on WITEC CRM200 confocal Raman spectrometer with a 532 nm laser source. Typically, a dispersion grating of 600 g mm-1 and a co-adding of 64 scans were applied in the spectral tests.

X-ray photoelectron spectroscopy was obtained with a Thermo Scientific K-Alpha ESCA spectrometer, using a monochromatic Al Kα radiation (1486.6 eV) and a low energy flood gun as neutralizer. The binding energy of C 1s peak at 284.6 eV were used as reference. The quantification method is based on measuring the peak area of each element on the sample surface, since the number of detected electrons in each of the characteristic peaks is directly related to the amount of element within the XPS sampling volume. To generate atomic percentage values, each raw XPS signal will be further corrected by dividing its signal intensity (number of electrons detected) by a "relative sensitivity factor" (RSF), and normalized over all of the elements detected. Thermo Avantage V5 program were employed for surface componential content analysis as well as peaks fitting for selected elemental scans.

The X-ray absorption spectroscopy (XAS) at Ni K-edge was used to study the electronic and coordination properties of Ni samples. The Ni K-edge spectra acquired using the SXRMB beamline of Canadian Light Source. The SXRMB beamline used an Si(111) double crystal monochromator to cover an energy range of 2−10 keV with a resolving power of 10000. The XAS measurement was performed in fluorescence mode using a 4-element Si(Li) drift detector in a vacuum chamber. The powder sample was spread onto doublesided, conducting carbon tape. Ni foil was used to calibrate the beamline energy. Analyses of both the near edge (in energy scale) and extended range (in R space) XAS spectra were performed using Athena software.

Powder X-ray diffraction data were collected using a Bruker D2 Phaser diffractometer in parallel beam geometry employing Cu Kα radiation and a 1-dimensional LYNXEYE detector, at a scan speed of 0.02° per step and a holding time of 1 s per step.

Electrochemical characterizations

The electrochemical measurements were run at 25 °C in a customized gastight H-type glass cell separated by Nafion 117 membrane (Fuel Cell Store). A BioLogic VMP3 work station was employed to record the electrochemical response. Certain amounts of $KHCO_3$ (Sigma-Aldrich, 99.95 %) was dissolved in Millipore water to prepare the 0.1 M and 0.5 M electrolyte, which was further purified by electrolysis between two graphite rods at 0.1 mA for 24 h to remove any trace amount of metal ions. In a typical 3-electrodes test system, a platinum foil (Beantown Chemical, 99.99 %) and a saturated calomel electrode (SCE, CH Instruments) were used as the counter and reference electrode, respectively. A fresh (electrochemically) polished glassy carbon (HTW GmbH, 1cm x 2cm), with its backside covered by an electrochemically inert, hydrophobic wax (Apiezon wax W-W100), was used as the working electrode substrate. Typically, 5 mg of as-prepared catalyst was mixed with 1 mL of ethanol and 100 μL of Nafion 117 solution (Sigma-Aldrich, 5 %), and sonicated for 20 min to get a homogeneous catalyst ink. 80 μL of the ink was pipetted onto 2 cm^2 glassy carbon surface (0.2 mg cm^{-2} mass loading), got vacuum dried prior to usage. The catalyst mass loading in Figures 2F and 2G was 1 mg/cm^2 on carbon fiber paper electrode (Fuel Cell Store). All potentials measured against SCE was converted to the reversible hydrogen electrode (RHE) scale in this work using $E\ (vs\ RHE) = E\ (vs\ SCE) + 0.244\ V + 0.0591*pH$, where pH values of electrolytes were determined by Orion 320 PerpHecT LogR Meter (Thermo Scientific). Solution resistance (R_u) was determined by potentiostatic electrochemical impedance spectroscopy (PEIS) at frequencies ranging from 0.1 Hz to 200 kHz, and manually compensated as $E\ (iR\ corrected\ vs\ RHE) = E\ (vs\ RHE) - R_u * I\ (amps\ of\ average\ current)$. OER tests were performed in 0.5 M $KHCO_3$ + 0.5 M K_2HPO_4/KH_2PO_4 buffer solution with pH of 7.5 under CO_2 saturation.

For the flow cell test,[3] 0.2 mg/cm^2 NiN-GS and IrO_2 were air-brushed onto two 1×2.5 cm^2 Sigracet 35 BC GDL (Fuel Cell Store) electrodes as CO_2RR cathode and OER anode, respectively. The two electrodes were therefore placed on opposite sides of two 0.5-cm thick PTFE sheets with 0.5-cm wide by 2.0-cm long channels such that the catalyst layer interfaced with the flowing liquid electrolyte (Figure S15). A nafion film was sandwiched by the two PTFE sheets to separate the chambers. The geometric surface area of catalyst is 1 cm^2. On the cathode side a titanium gas flow chamber supplied 5 sccm CO_2 while the anode was open to the atmosphere. The flow rate of 1M $KHCO_3$ electrolyte (pH 8.4) was 0.5 sccm in both chambers controlled by a syringe pump. SCE was used as the reference electrode.

Artificial photosynthesis test

In the 3D-printed electrosynthetic cell (Figure S35) for fuel production, 0.5 M $KHCO_3$ and 0.5 M $KHCO_3$ + 0.5 M K_2HPO_4/KH_2PO_4 buffer solution (both saturated with CO_2 with pH of 7.5) were used in the cathodic compartment for CO_2 reduction and anodic compartment for OER, respectively. The mass loadings of NiN-GS and Li-Co_3O_4 are 0.3 and 8 mg on 1 cm^2 glassy carbon and CFP electrode, respectively. The 1 cm^2 $GaInP_2$/GaAs/Ge TJ solar cell was illuminated under AM 1.5G 0.5 Sun solar simulator (Newport, calibrated by Newport reference cell) to match the current density of the electrosynthetic cell (~ 5 mA/cm^2 working current). The positive electrode of the solar cell was connected with Li-Co_3O_4 and the negative with NiN-GS, respectively. One channel of electrochemical working station was wired in parallel to monitor the voltage and another one was wired in series (with 0 V applied) to monitor the current. A mini magnet stirring bar was added in the cathode chamber of the 3D-printed electrosynthetic cell to dramatically facilitate the electrolyte mass transport. Trace amount of Co ions from the OER catalyst surface could be leached out into the electrolyte due to the local pH decrease during long-term OER electrolysis. Trace amount of Co ions diffusing across the nafion membrane can be deposited as Co metal onto the cathode due to the negative potential applied,[4] which poisons the CO_2RR catalyst and decreases the CO FE and thus the overall SFE. Therefore, we refreshed the electrolyte in the electrosynthetic cell every few hours (shown as the spikes in the current density in Figure S36e) to avoid metal ion contaminations in CO_2 reduction. Both the mass transport and the cross-contamination issues can be further improved by designing a flow cell for real applications in the future.

CO_2 reduction products analysis

During electrolysis, CO_2 gas (Airgas, 99.995 %) was delivered into the cathodic compartment containing CO_2-saturated electrolyte at a rate of 50.0 standard cubic centimeters per minute (sccm, monitored by Alicat Scientific mass flow controller) and vented into a gas chromatograph (GC, Shimadzu GC-2014) equipped with a combination of molecular sieve 5A, Hayesep Q, Hayesep T, and Hayesep N columns. A thermal conductivity detector (TCD) was mainly used to quantify H_2 concentration, and a flame ionization detector (FID) with a methanizer was used to quantitative analysis CO content and/or any other alkane species. The detectors are calibrated by two different concentrations (H_2: 100 and 1042 ppm; CO: 100 and 496.7 ppm) of standard gases (Figure S8). The gas products were sampled after a continuous electrolysis of ~ 15 min under each potential. The partial current density for a given gas product was calculated as below:

$$j_i = x_i \times v \times \frac{n_i F p_0}{RT} \times (electrode\ area)^{-1}$$

where x_i is the volume fraction of certain product determined by online GC referenced to calibration curves from two standard gas samples (Scott and Airgas), v is the flow rate of 50 sccm, n_i is the number of electrons involved, p_0 = 101.3 kPa, F is the Faradaic constant and R is the gas constant. The corresponding Faradaic efficiency (FE) at each potential is calculated by $FE = j_i/i_{total} \times 100\,\%$. A representing example to demonstrate the whole process of FE measurement is shown in Figure S8. We held the potential at – 0.82 V vs RHE (the highest CO FE) for a continuous electrolysis with a 50 sccm CO_2 gas flow. The chronoamperometry current is shown as Figure S8b with a current density ~ 4.34 mA/cm^2 (1 cm^2 electrode for test). The 50 sccm CO_2 gas, mixed with continuously produced H_2 and CO, continuously flowed through the sampling loop (1 mL) of GC during the electrolysis. At ~ 15 min the GC machine automatically switched valves to inject the gas sample in the sampling loop into packed columns for analysis. H_2 was detected by TCD at ~ 5.5 min (Figure S8c), and CO was first converted into CH_4 by methanizer and then detected by FID at ~ 11 min (Figure S8d). Based on the GC calibration curve (Figures S8e and S8f) and the integrated peak areas of H_2 and CO, we obtained the concentration of H_2 to be ~ 74 ppm and CO ~ 616.7 ppm. With a 50 sccm CO_2 flow, the gas products were therefore produced at a rate of 2.57×10^{-9} mole/s of H_2 and 2.14×10^{-8} mole/s of CO, which corresponds to a partial current density of 0.49 mA/cm^2 H_2 and 4.13 mA/cm^2 CO. The corresponding FEs were finally obtained as 11.3 % of H_2 and 95.2% of CO. The cumulated gas volume during the 15-min electrolysis is 0.055 mL for H_2 and 0.462 mL for CO. A few advantages of the CO_2 gas flow cell method for GC measurements are: 1) the gas product concentration can be tuned by changing the CO_2 gas flow rate and therefore the FE measurements can be accurate even for small currents; 2) the gas sample injection by auto GC valve switching can be highly dependable with small error ranges; 3) by programming the GC auto valve switching every certain amount of time, the electrolysis can be continuously operated and analyzed for long-term stability test unattended.

1D ^{1}H NMR spectra were collected on an Agilent DD2 600 MHz spectrometer to test if any liquid products present during the CO_2 reduction over NiN-GS catalyst. Typically, 900 μL of electrolyte after electrolysis (or 0.1 M $KHCO_3$ containing certain chemicals of interest) were mixed with 100 μL of D_2O (Sigma-Aldrich, 99.9 at% D) and 0.05 μl dimethyl sulfoxide (Sigma-Aldrich, 99.9 %) as internal standard.

Isotope labeling

^{13}C isotope measurements were run on Agilent 7890A GC-MS equipped with a thermal conductivity detector and an Agilent 5975C inert Triple-Axis quadrupole mass selective detector. $^{13}CO_2$ (Sigma-Aldrich, 99 at% ^{13}C) stream was delivered into the cathodic

compartment containing 0.1 M $NaHCO_3$-^{13}C (Sigma-Aldrich, 98 at% ^{13}C) at a rate of 20 sccm and was routed into the GC-MS with He as the carrier gas.

Density functional theory calculations

Electronic structure calculations were performed using the Quantum ESPRESSO program package,[5] integrated with the Atomic Simulation Environment (ASE).[6] The electronic wavefunctions were expanded in series of plane waves with a cutoff energy of 500 eV and an electron density cutoff of 5000 eV. Core electrons were approximated with ultrasoft pseudopotentials.[7] We used the BEEF-vdW exchange-correlation functional,[8] which has been shown to accurately describe chemisorption as well as physisorption properties on graphene. For adsorption studies, a supercell of lateral size (7x7) was used to account for 1% impurity of Ni in graphene lattice, and a vacuum region of at least 18 Å is used to decouple the periodic images. The first Brillouin zone was sampled with (3x3x1) Monkhorst-Pack *k*-points.[9] All atoms were allowed to relax until the maximum force on each atom was below 0.05 eV/A for each calculation. To account for the magnetism of the Ni dopants in the graphene lattice, we applied the model developed by Krasheninnikov *et al.*,[10] for metal dopants at single (M@SV) and double vacancies (M@DV) of graphene layers. All calculations were performed with spin polarization.

The CHE method introduced in Ref. 11 was used to calculate the free energy levels of all adsorbates. In this model, chemical potential of proton-electron pair equated with that of gas-phase H_2 at 0 V *vs.* RHE, and the electrode potential is taken into account by shifting the electron energy by $-eU$, where e and U are the elementary charge and the electrode potential, respectively. We define the thermodynamic limiting potential of electrochemical reactions to be the negative of the maximum free energy difference between any two successive electrochemical steps. The reaction energies of each individual intermediate are calculated and corrected by zero-point energy (ZPE) and entropy (TS) using the following equation:

$$\Delta G = \Delta E + \Delta ZPE - T\Delta S$$

We apply the ZPE and TΔS values reported by Peterson et al., (*Energy Environ. Sci.* 2010, 3, 1311), with an additional adsorption energy correction of 0.3 eV for *COOH intermediate to account for solvation effect as recommended by Tripkovic et al. (*J. Phys. Chem. C* 2013, 117, 9187) in Figure S28.

Supplemental Notes

Estimation of TOF and TON

The calculation of TOF and TON per site was based on the estimation of the numbers of Ni active sites in NiN-GS catalysts. First of all, the surface area of the graphene layers in NiN-GS catalyst can be estimated by the electrochemical double layer capacitance (EDLC). Based on previous literatures, the EDLC of graphene is measured to be ~ 21 μF cm^{-2} on one side.[12-13] This is very close to the glassy carbon electrode capacitance (24 μF cm^{-2}, Figure S17) we measured here. Since the EDLC of NiN-GS catalyst is 1.57 mF (0.2 mg loading on 1 cm^2 geometric electrode area), and regardless of the effects of the trace amount of Ni or N in the graphene layers (the EDLC of Ni-GS is quite similar to NiN-GS, confirming our hypothesis), we could estimate the surface area of graphene layers in NiN-GS to be ~ 75 cm^2. Therefore the moles of carbon atoms on the electrochemical surface can be calculated to be 75/10000 m^2 / 2600 m^2 g^{-1} / 12 g mol^{-1} = 2.4*10^{-7} mol, where 2600 m^2 g^{-1} is the theoretical specific surface area of graphene.[12] Based on the XPS measurement where signals from surface Ni atoms in the graphene shell become dominant in NiN-GS (Figure S6), the atomic ratio of Ni atoms is ~ 1 %. Since we cannot completely rule out the small contribution from Ni NPs embedded below, this atomic ratio could be a slightly overestimation of the Ni atom concentrations in the graphene shell, which could result in an underestimation of the TOF and TON per site. This gives us the moles of Ni sites in the surface graphene layers to be ~ 2.4*10^{-9} mol. The partial current of CO_2 reduction to CO on NiN-GS under an overpotential of η = - 0.7 V is ~ 4 mA, which gives us a TOF of Ni active site to be 4/1000 C s^{-1} / 10^5 C mol^{-1} / 2 / 2.4*10^{-9} mol = 8 s^{-1} = 28800 h^{-1}. The cumulative TON was calculated based on the long-term electrolysis in Figure 2D.

Formation energies of different atomic structures

We calculated the formation energies of the Ni atom doped in the single and double vacancies of graphene as follows:

$$\Delta E_f = E_{Ni@v} - E_v - E_{Ni}(bulk), \quad \text{(a)}$$

where ΔE_f is the formation energy of the Ni-doped graphene, $E_{Ni}(bulk)$ the chemical potential of Ni atom in the bulk metal, and E_v the energy of bare graphene with a single or double vacancy. The calculated formation energies for Ni@SV and Ni@DV are – 2.33 and – 2.10 eV which show Ni atomic sites in graphene vacancies to be chemically very stable. A variety of possible Ni and N co-doped single (Figure S27a) or double vacancies (Figure S27b) in graphene were also investigated. Different N coordination around Ni@SV or Ni@DV show varied stabilities. In order to investigate the stability of each N

configuration, we calculated the relative formation energies ΔE_f of different N coordination structures using the following:

$$\Delta E_f = E_{Ni-nN} - E_{Ni-nC} - nE_{NH3} + n_C\mu_C + 3n/2E_{H2}. \quad (b)$$

where E_{Ni-nN} is the energy of the N-doped in Ni@SV or Ni@DV, E_{Ni-nC} is the related energies of Ni@SV or Ni@DV, E_{NH3} is the energy of the gas phase ammonia, and μ_C is the chemical potential of carbon. The results are listed in Table S3. In general, the more stable configurations are those where N forms a direct bond to the Ni.

Constructing artificial photosynthesis system

Considering the significant energy loss by the low ionic conductivity in 0.1 M $KHCO_3$ electrolyte, we hereafter increase the salt concentration to 0.5 M (pH 7.5 under CO_2 saturation) in the full cell system to reduce the *iR* drop while maintaining a high FE of CO_2 to CO on NiN-GS catalyst (Figure S31, Supplemental Methods). Relatively small OER overpotentials in alkaline solutions have been achieved by TM catalysts,[14-15] which however do not work well in neutral pH.[16] Co-based catalytic materials usually perform better than other TMs in neutral pH but still need ~ 500 mV overpotential to deliver 5 to 10 mA/cm^2 current.[17-20] Inspired from studies in TM oxide Li ion batteries, where electrode materials gradually fracture due to the cyclic Li^+ insertion and extraction, we Li^+ tuned Co_3O_4 catalyst (Li-Co_3O_4) to create additional grain boundaries and active sites for neutral pH OER (Figure S32, Supplemental Methods).[14] The sizes of pristine Co_3O_4 NPs (~ 100 nm) were significantly reduced after the Li tuning process as observed by SEM images (Figure S33). In addition, the X-ray diffraction (XRD) pattern of Co_3O_4 disappears in Li-Co_3O_4 (Figure S34), which confirms that ultra-small grains below the detection limit of XRD have been created within the NPs.[14] As a result, the OER catalytic activity of Li-Co_3O_4 was dramatically improved from the pristine sample (Figure S36a).[21] An OER electrolysis of Li-Co_3O_4 under 5 mA/cm^2 current, which matches the current of the best CO FE of NiN-GS catalyst (Figure S31), can be continuously operated at ~ 1.6 V *vs.* RHE (370 mV overpotential) for more than 20 hours with negligible degradation (Figure S36b). Considering the NiN-GS CO_2 reduction catalyst with a – 0.74 V *vs.* RHE potential for ~ 87 % CO FE, the full-cell reaction can be operated under 2.34 V (without considering the *iR* drop) and deliver a ~ 50 % electricity to CO energy conversion efficiency. This optimized operation voltage, added with additional ohmic loss (Figure S35), can be powered by a single cell of commercialized $GaInP_2$/GaAs/Ge TJ photovoltaic which delivers an open-circuit voltage to more than 2.5 V (Figures S36 and S37).[22] An artificial photosynthesis system was therefore built by integrating a 1 cm^2 TJ solar cell with the NiN-GS and Li-Co_3O_4 catalysts in a 3D-printed electrosynthetic cell (Figures S35 and S36c), under simulated solar illumination and without any external power input. To match the 5 mA/cm^2 working current in the electrolytic system, the 1

cm^2 solar cell was illuminated under AM 1.5G 0.5 Sun (Supplemental Methods). The electrolyte was refreshed every few hours to avoid metal ion deposition onto CO_2 reduction catalyst (Supplemental Methods). The efficiency of solar-to-CO (STC) is calculated by the equation of $\eta_{STC} = j_{tot} \times FE_{CO} \times 1.35V/P_{solar}$ where 1.35 V represents the thermodynamic energy of CO_2 to CO conversion and P_{solar} is the input power of solar energy. Over 10 % artificial photosynthesis efficiency can be maintained with earth-abundant electrocatalysts (Figure S36e) over 10-hour continuous operation, exceeding that of biological photosynthesis in nature [23]. The STC efficiency can likely be further improved with more advanced integrated system (instead of the direct wiring here) to ensure the optimized operation voltage for both the photovoltaic device and electrolytic cell. The limitations for direct wiring here is: the optimized working voltage and current of the solar cell and electrosynthetic cell does not match each other. A few improvements can be expected: 1) constructing integrated solar panels and integrated electrosynthetic cells to match the voltage and current of the two-different systems; 2) employing high-efficiency maximal power point tracking (MPPT) system and voltage convertor between the solar and electrosynthetic cells; 3) fine tuning the loading and electrode area of both CO_2 reduction and OER catalysts to match the working voltage and current with the solar cell. Considering a well-matched integration of commercial solar cell system (~ 20 % efficiency) and our CO_2 electrolytic system (~ 50 % efficiency), ~ 10 % artificial photosynthesis can be achieved in practical applications in the future.

Supplemental Figures

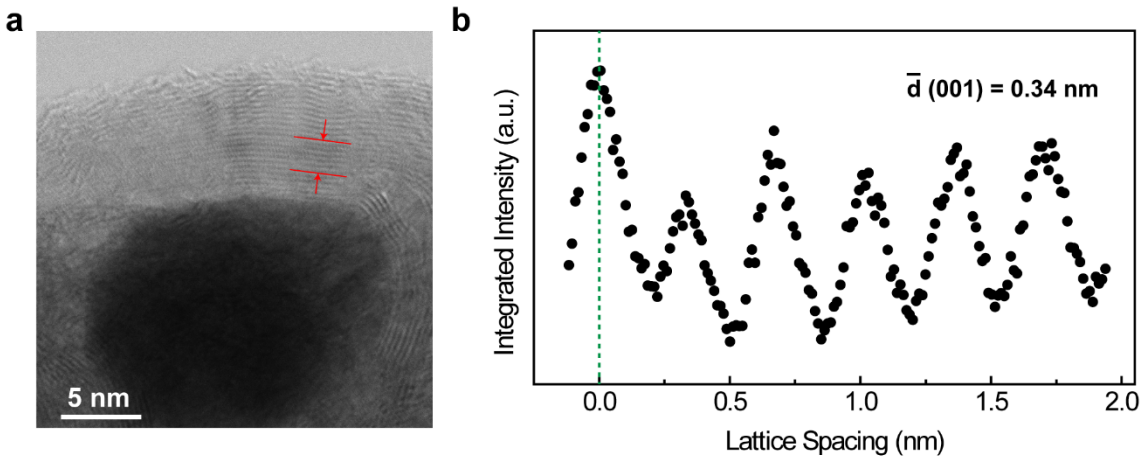

Figure S1.

The measurement of graphene layer spacing by STEM. The arrows in (a) indicate the region for spacing analysis. (b) represents the integrated pixel intensities of graphene layers along (001) spacing directions (which is perpendicular to the facets). The peaks and valleys represent the atoms and gaps, respectively. The layer spacing of 0.34 nm is averaged over 6 atomic layers for high accuracy, which is very close to the 0.335 nm spacing reported in literature [24].

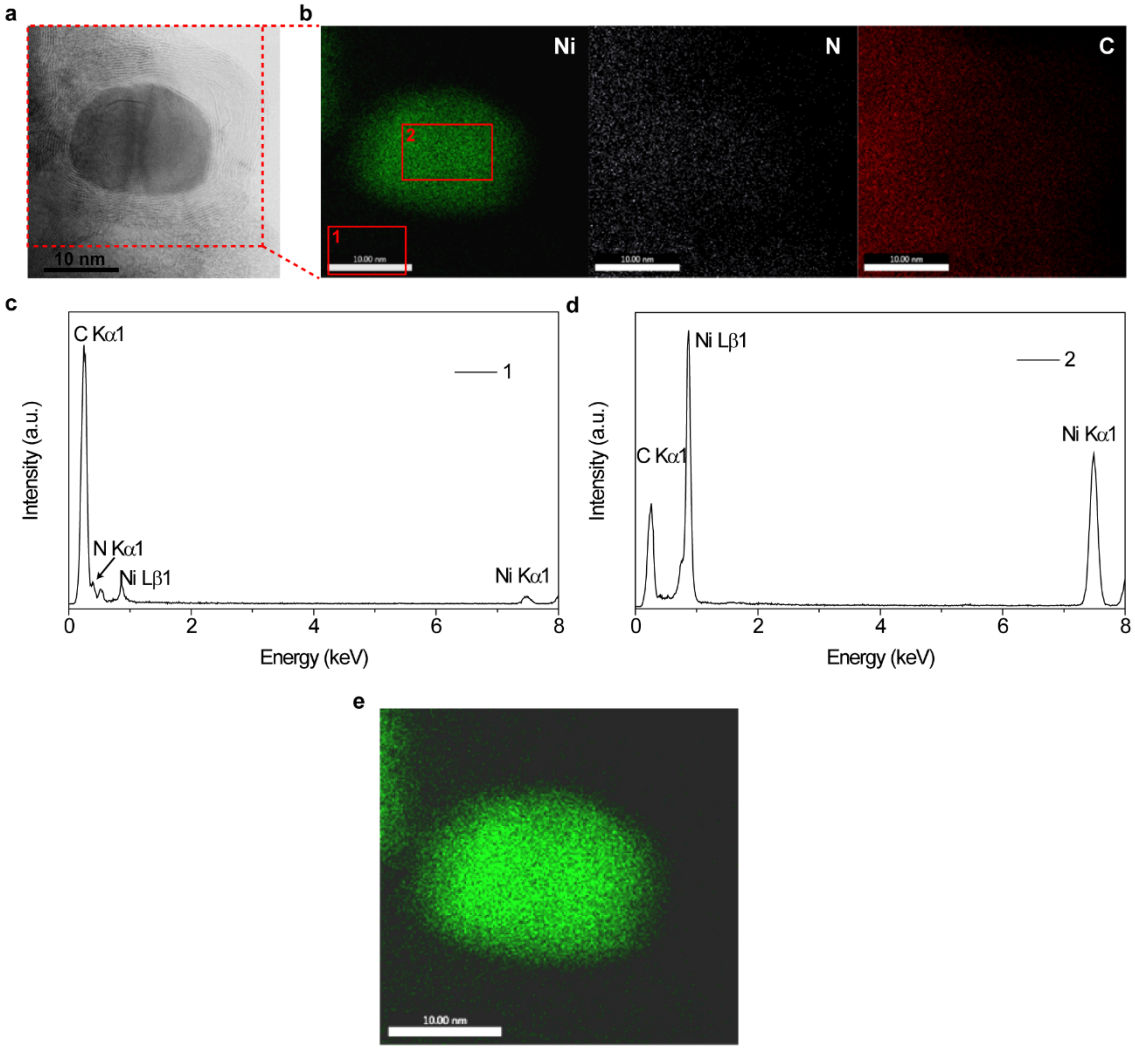

Figure S2.

EDS mapping of NiN-GS. (a) STEM image of NiN-GS. (b) EDS mapping of Ni, N and C. Due to the high contrast, the Ni signals represented by green dots in the surrounding graphene shell is not that obvious. (c, d) The corresponding EDS spectra of selected areas in Ni mapping. Ni peaks were observed in the area 1 of graphene shells. (e) Enhanced Ni EDS signals in the GS region after tuning of the image contrast.

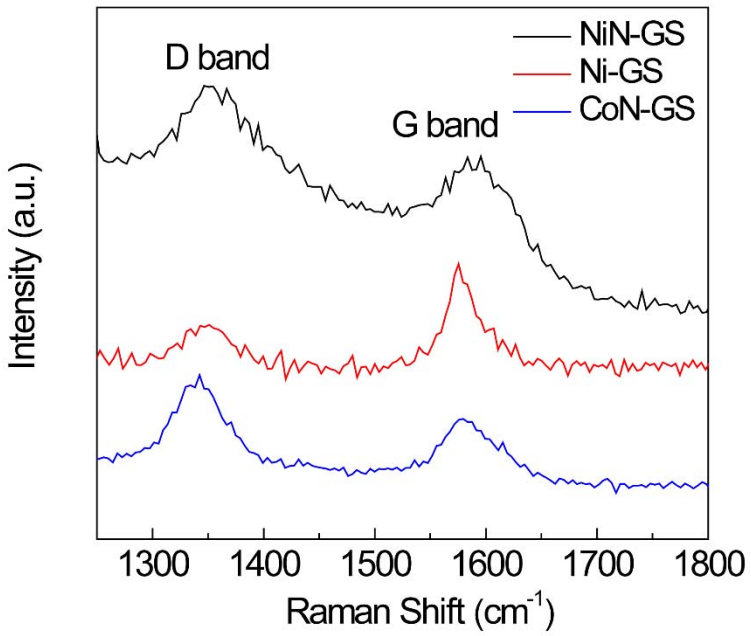

Figure S3.

Raman spectra of NiN-GS, Ni-GS, and CoN-GS catalysts. The distinguished peaks at ~ 1350 and 1580 cm^{-1} are assigned to defected graphite (D band) and graphite (G band) features, respectively. The much higher peak intensity ratio of D to G band in NiN-GS compared with Ni-GS suggests that the N incorporation helps to create a significant number of defects in the graphene shell.

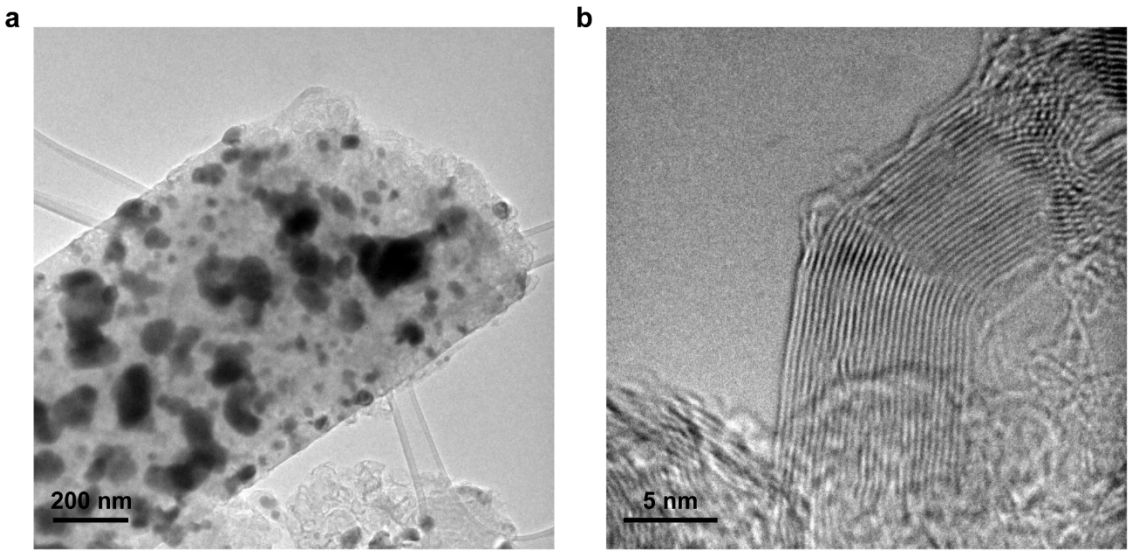

Figure S4.

TEM characterizations of Ni-GS. The graphene layers in (b) shows less curvatures and defects compared with NiN-GS in Figure 1A, Figures S2a and S16b.

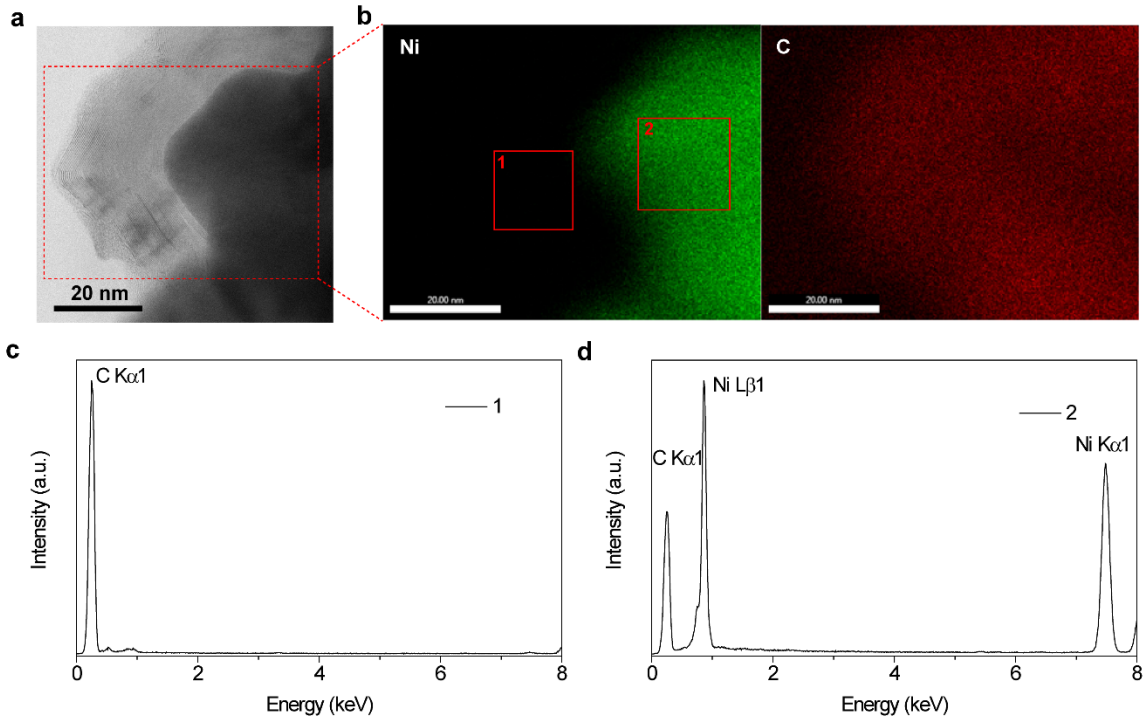

Figure S5.

EDS mapping of Ni-GS. (a) STEM image of Ni-GS. (b) EDS mapping of Ni and C. (c, d) The corresponding EDS spectra of selected areas in Ni mapping. Negligible Ni peaks were observed in the area 1 of graphene shells.

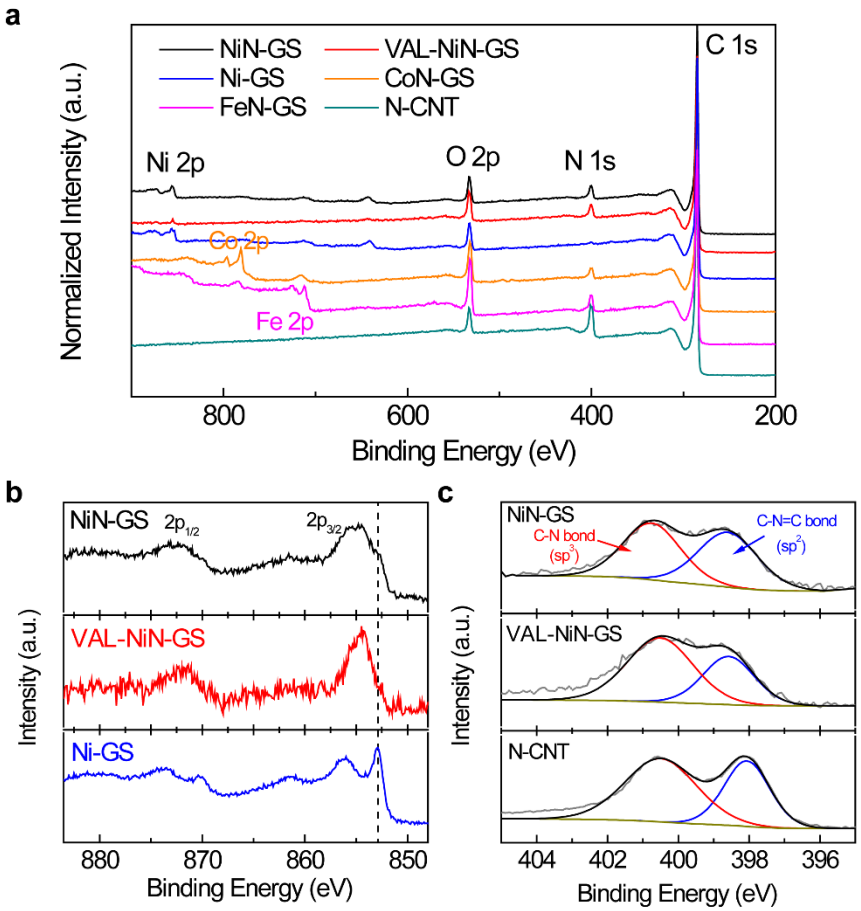

Figure S6.

XPS characterization. (a) Normalized XPS survey spectra of NiN-GS, VAL-NiN-GS, Ni-GS, CoN-GS, FeN-GS, and N-CNF. (b) XPS spectra of Ni 2p regions of NiN-GS, VAL-NiN-GS, and Ni-GS. The Ni $2p_{3/2}$ peak in Ni-GS indicated by the dash line is consistent with Ni metals, which is contributed by the Ni NPs embedded below [25]. In the case of NiN-GS, since the sampling depth for XPS with AlKα radiation is ~ 3 to 10 nm [26], the Ni atoms trapped in the surface graphene shells (~ 5 to 10 nm thick) could contribute much strongly XPS signals than those deeply embedded NPs. As a result, NiN-GS shows a large portion of positively shifted binding energies (due to the coordination with carbon) in addition to the Ni NP signals. This is further confirmed by the Ni XPS spectrum of VAL-NiN-GS sample where only a portion of Ni atoms trapped in the graphene shell, but not those Ni NPs embedded, were remained after the violent acid leaching process. The possible Ni-N coordination in the graphene shell may also contribute to the higher oxidation states. (c) XPS spectra of N 1s regions of NiN-GS, VAL-NiN-GS, and Ni-GS. The ratio of pyridinic N in N-CNF is slightly more than that of NiN-GS and VAL-NiN-GS.

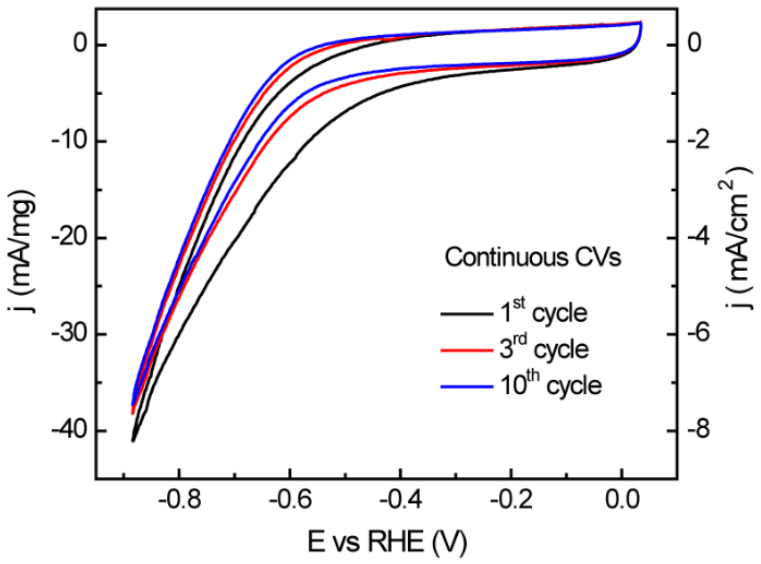

Figure S7

Continuous cyclic voltammograms of NiN-GS in CO_2 saturated 0.1 M $KHCO_3$ solution. In contrast to overlapped sweep currents for HER shown in Figure 2A under N_2 saturated electrolyte, an evident hysteresis of forward- and backward-scan voltammograms is observed for CO_2 reduction. The slightly higher current density in the first CV cycle is due to the reduction of some surface bonded oxygen.

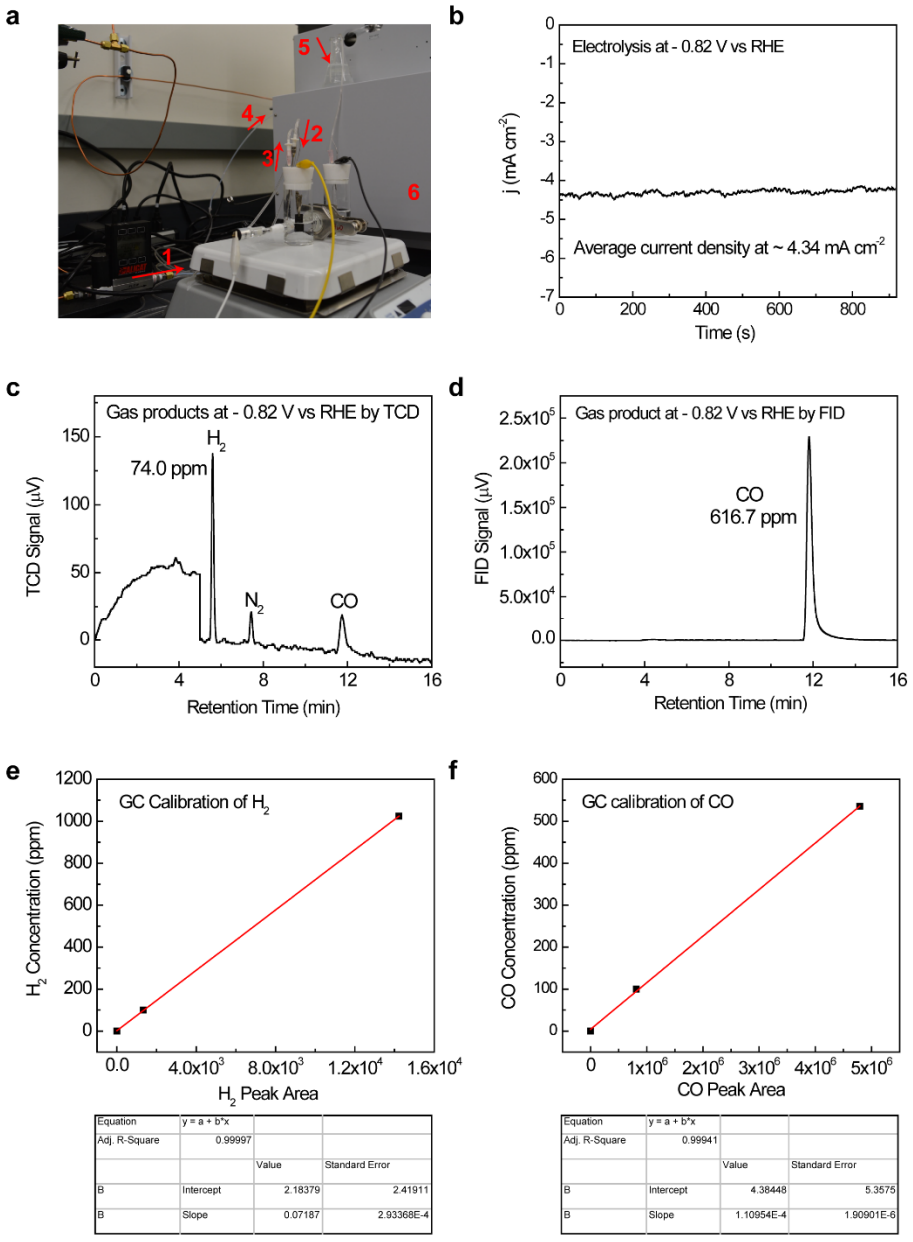

Figure S8

The GC measurement set up and a representing example to demonstrate the whole process of FE measurement. (a) 1. Mass flow control (MFC) for an accurate 50 sccm CO_2 flow rate. 2. CO_2 gas flows into the cell. 3. CO_2 gas flows out of the reactor bringing gas products together. 4. The gas mixture fills the sampling loop of GC continuously. 5. The continuous gas flow is monitored by the bubbles generated in the glass. (b) Chronoamperometry of CO_2 reduction under -0.82 V vs RHE. (c, d) TCD and FID responses to the gas products. (e, f) TCD and FID standard gas calibration.

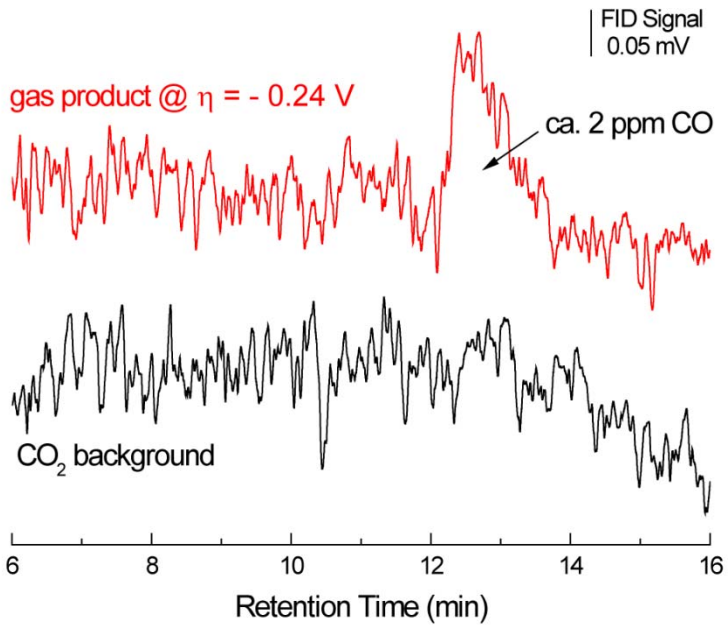

Figure S9.

Onset potential investigation for CO evolution on NiN-GS. FID spectra of 20 sccm CO_2 flow through H-Cell without potential control (black line) and with potential hold at 0.35 V vs RHE (red line) of NiN-GS sample. Depending on the detection limit of FID detector in GC we can conclude that the overpotential for the onset of CO_2 to CO reduction should be less than 230 mV.

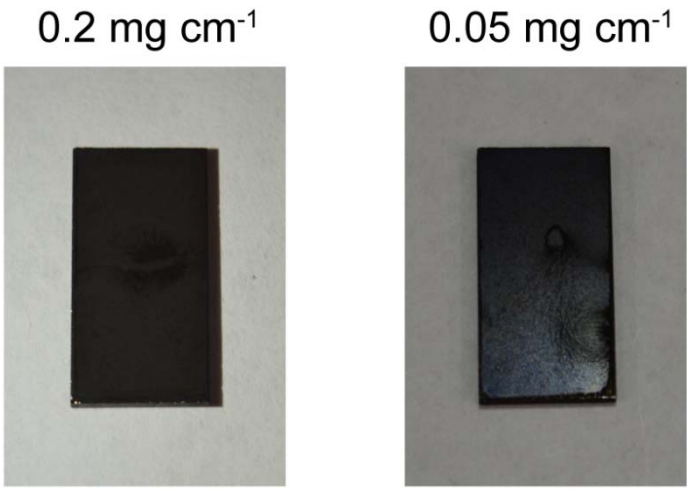

Figure S10.

Photographs of NiN-GS catalyst layer on glassy carbon electrode with different mass loadings. A loading of 0.2 mg cm^{-2} can form a uniform catalyst layer. Small loading of the catalyst results in exposed carbon electrode which can contribute significant H_2 evolution under CO_2 reduction conditions, and large mass loading on this flat surface presents a thick catalyst layer, where the mass transport could become limited for the catalyst buried beneath. Therefore, a suitable mass loading can best present the intrinsic activity of NiN-GS catalyst and thus provide the most accurate information for evaluating the catalytic active sites.

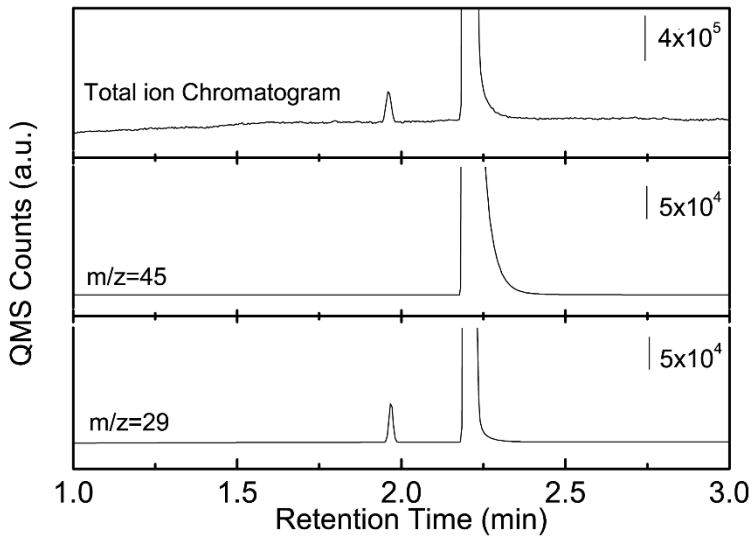

Figure S11.

GC-MS spectra recorded during isotope $^{13}CO_2$ electrolysis over NiN-GS at - 0.82 V vs RHE. The main peak at ca. 2.2 min is arising from $^{13}CO_2$ background, and the shoulder peak at ca. 1.9 min can be ascribed to the generation of ^{13}CO as reduction product, confirming that CO_2 stream is the main carbon source fed to be reduced.

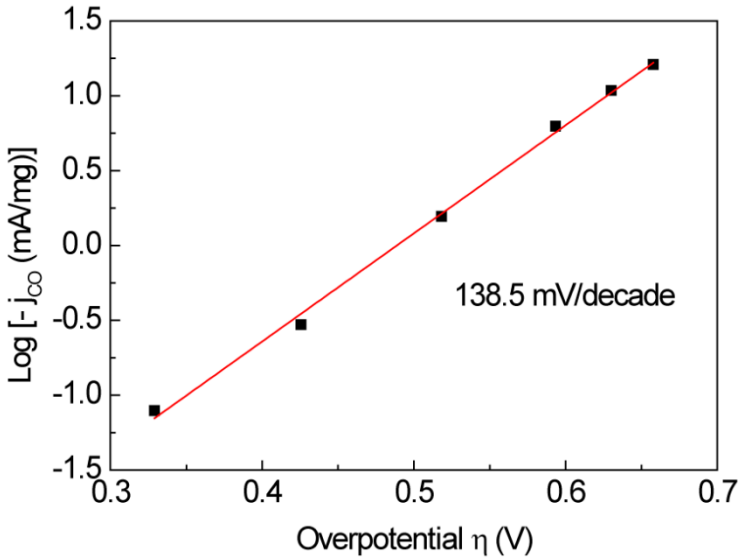

Figure S12.

The Tafel slope of CO evolution on NiN-GS catalyst. The currents are averaged over electrolysis currents.

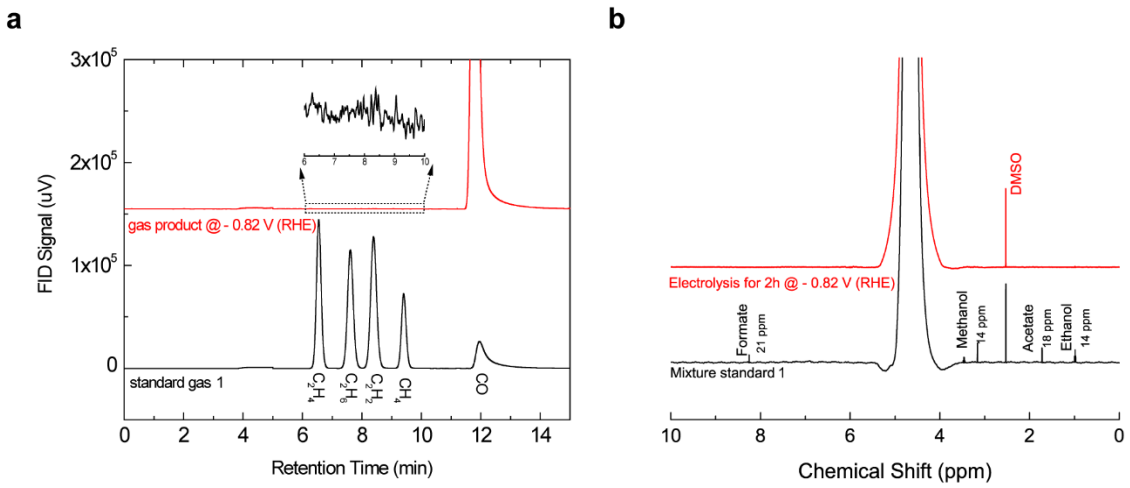

Figure S13.

CO_2RR products analysis. (a) Typical GC-FID spectrum recorded during CO_2 electrolysis over NiN-GS at - 0.82 V vs RHE (red line) together with a reference spectrum of standard mixture gas (black line at bottom) containing 101 ppm of C_2H_4, 100 ppm of C_2H_6, 100 ppm of C_2H_2, 100 ppm of CH_4, and 100 ppm of CO. Insert is a zoomed-in region of the former, representing no other gas products were detected. (b) ^1H NMR spectra of any reduction product after 2h electrolysis at - 0.82 V vs RHE over NiN-GS, together with a standard sample of 0.1 M $KHCO_3$ containing a mixture of species at low concentrations. No detectable liquid products were produced during the CO_2 to CO conversion process on NiN-GS catalysts.

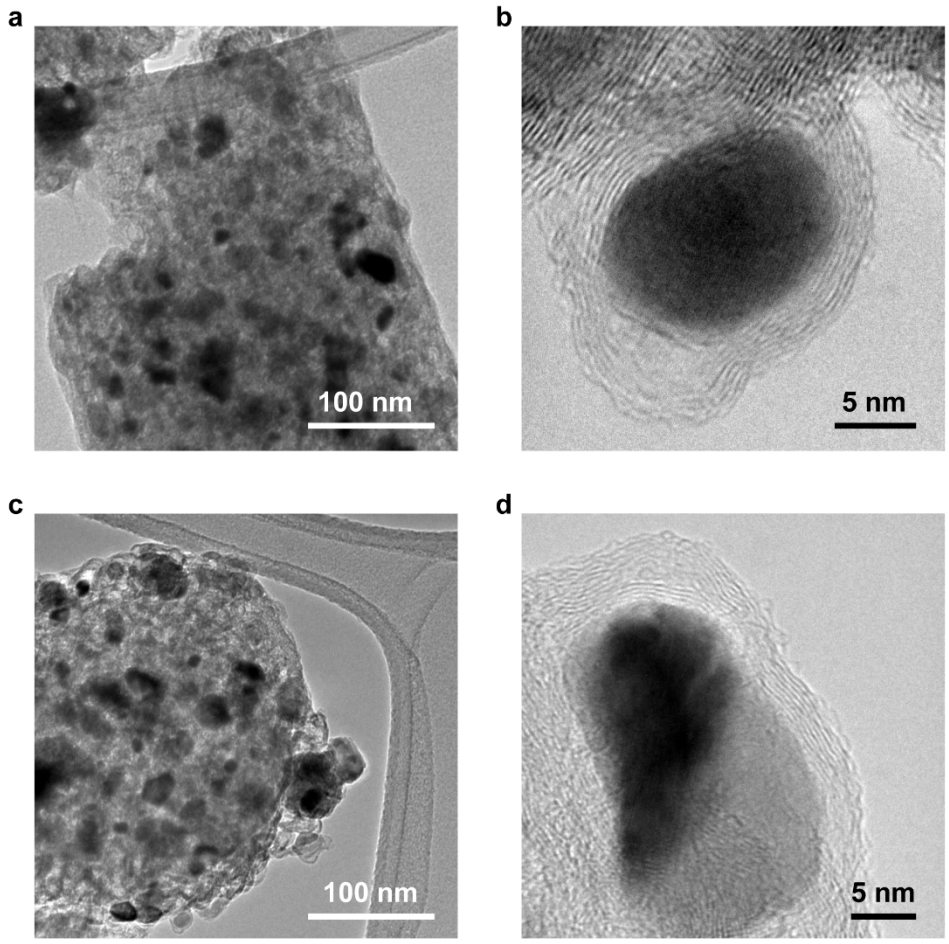

Figure S14.

TEM characterization of NiN-GS after long-term stability test. TEM images of NiN-GS before (a and b) and after (c and d) 20 h continuous electrolysis under – 0.7 V CO_2 to CO overpotential. The graphene shell is very robust and does not show any damages after the long-term electrolysis. No Ni NP aggregations were observed in the graphene shell region, suggesting the stability of those coordinated Ni single atoms.

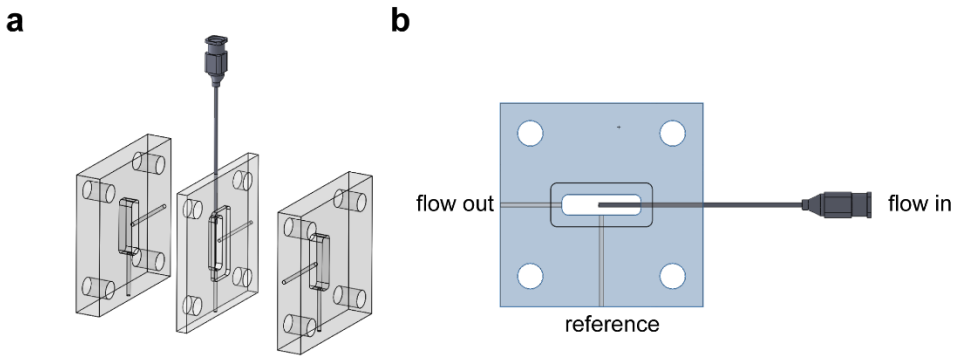

Figure S15

Flow cell test of NiN-GS catalyst on GDL electrode. (**a**) Schematic of the expanded view of the flow cell design. (**b**) Top view of the PTFE sheet for electrolyte flow.

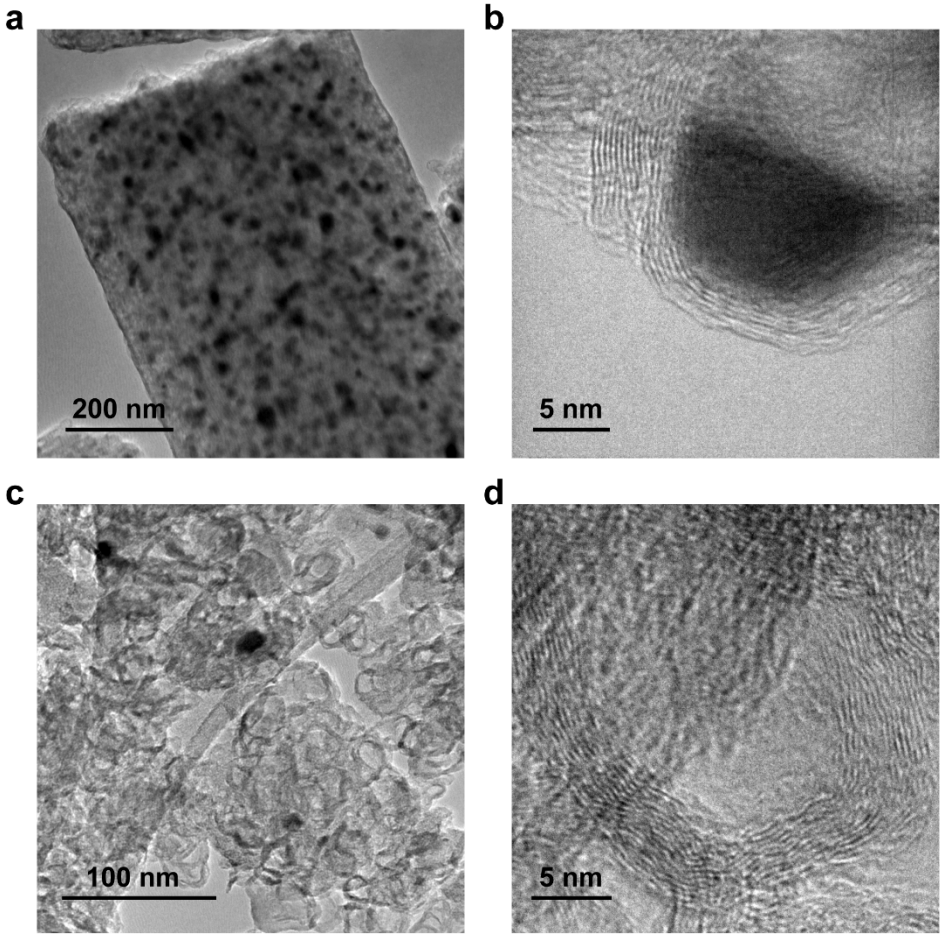

Figure S16.

TEM images of NiN-GS catalysts after acid leaching (a, b) and violent acid leaching (c, d) processes. The embedded Ni NPs cannot be leached away until the CNF was broken into small pieces with pin holes introduced to graphene shells as shown in (c). This shell protection can prevent the direct contact between Ni NPs and water.

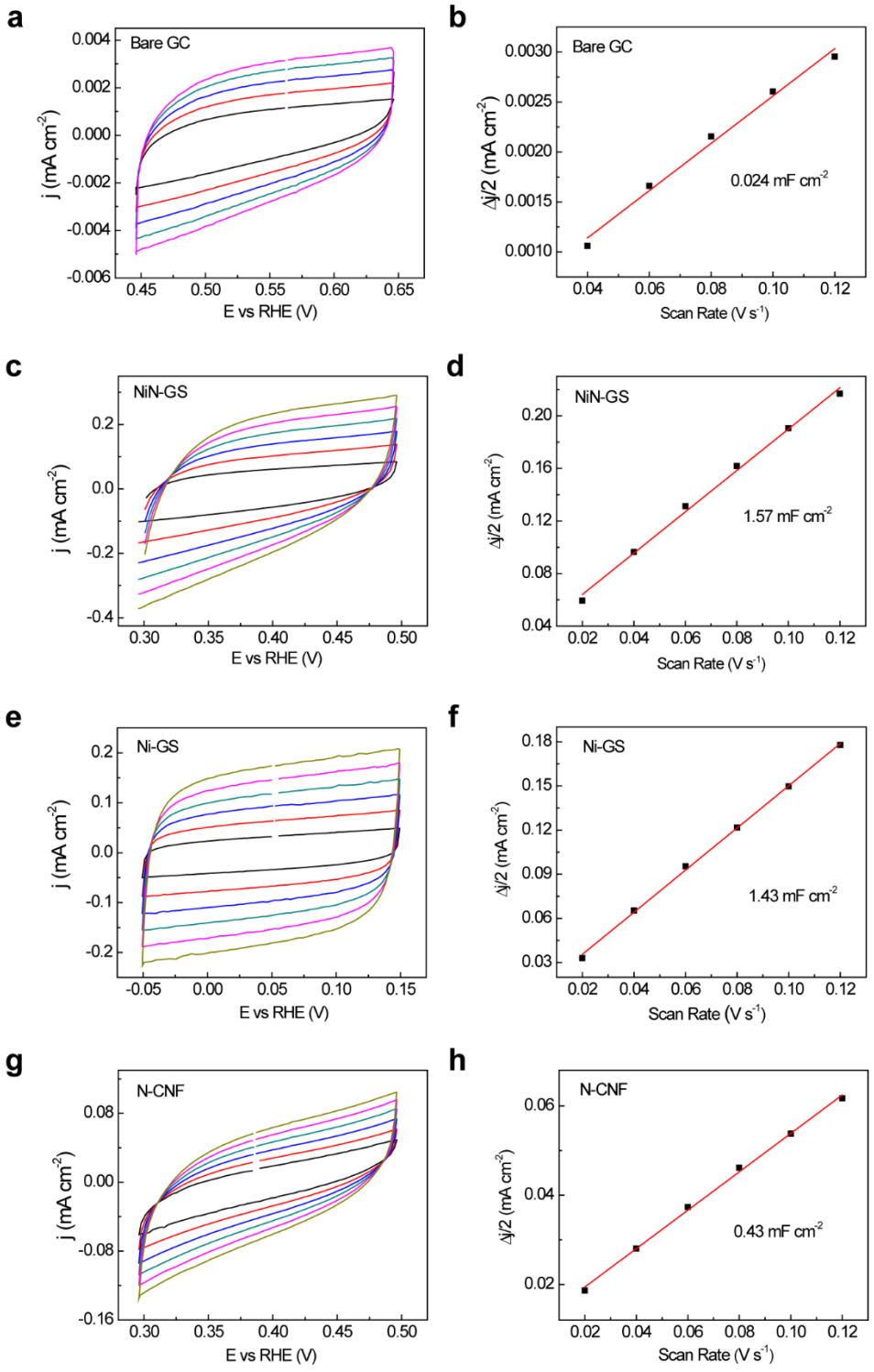

Figure S17.

EDLC measurements for bare glassy carbon electrode (a, b), NiN-GS (c, d), Ni-GS (e, f), and N-CNF (g, h).

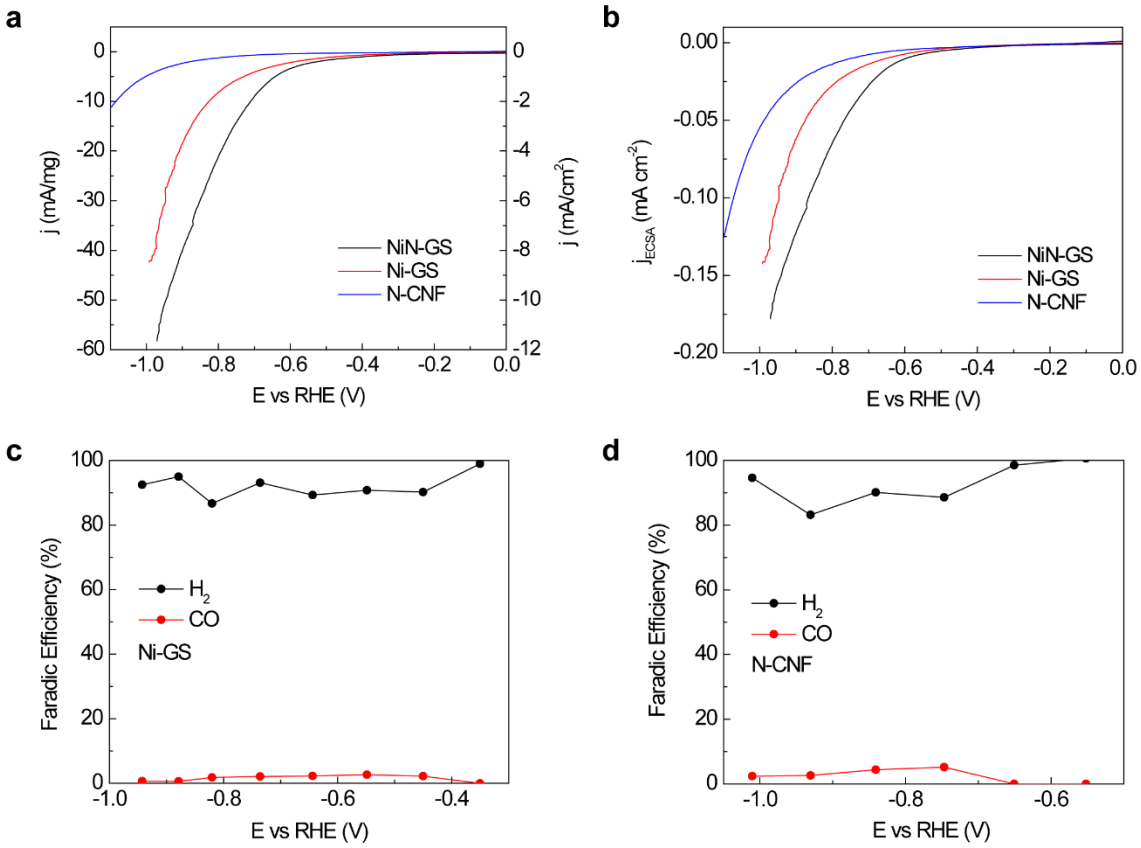

Figure S18.

Catalytic performances of Ni-GS and N-CNF. H_2 is the dominant product for both of them.

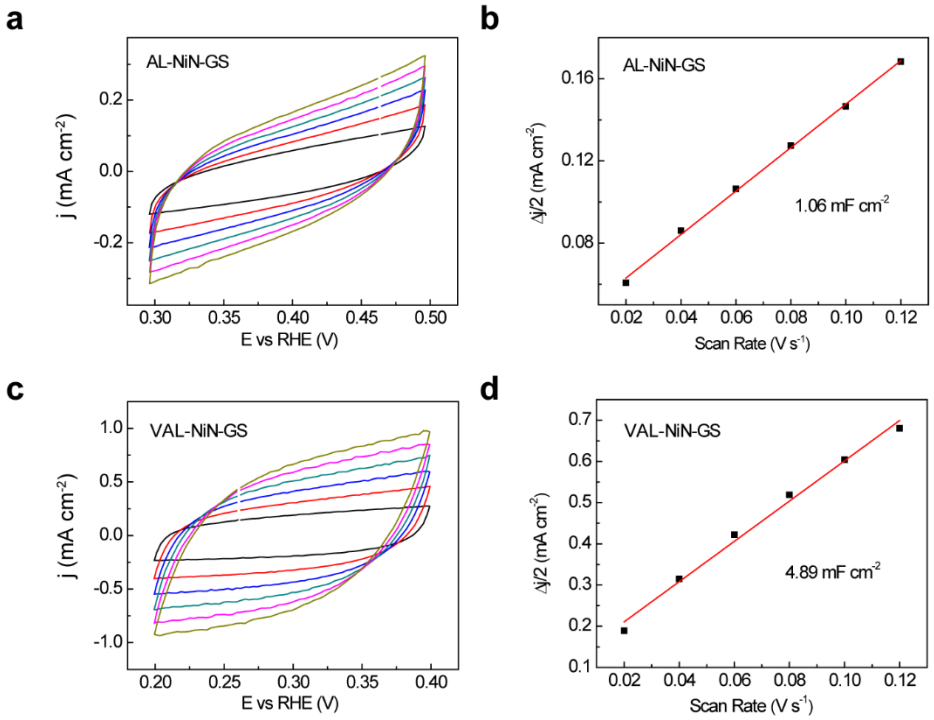

Figure S19.

EDLC measurements for AL-NiN-GS (a, b), and VAL-NiN-GS (c, d). The significantly increased capacitance of VAL-NiN-GS is due to the violent ball milling which greatly increases the surface area of the catalysts with the same mass loading on electrode.

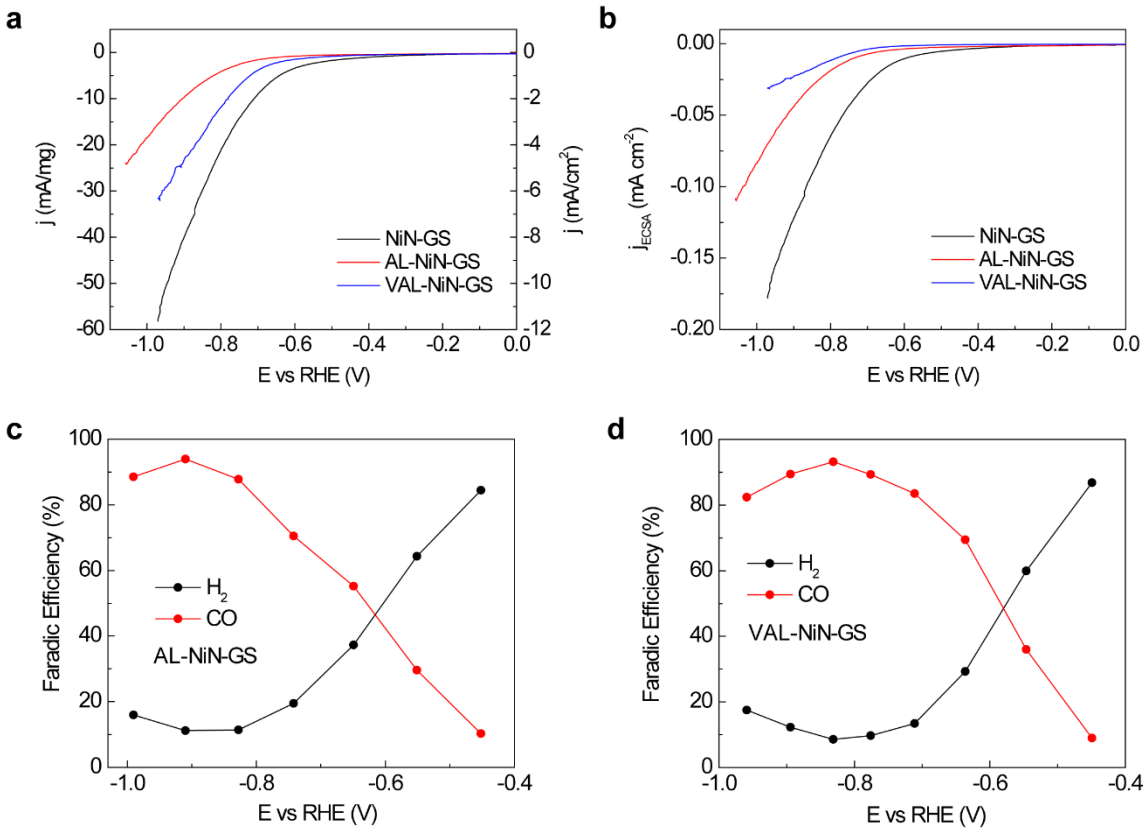

Figure S20.

Catalytic performances of catalysts after acid leaching processes. While the high CO FEs are maintained, the CO evolution currents are significantly decreased compared with the pristine sample. This might due to the incomplete acid leaching of Ni atoms in the graphene layers, as also evidenced by the XPS Ni signals from VAL-NiN-GS in Figure S6.

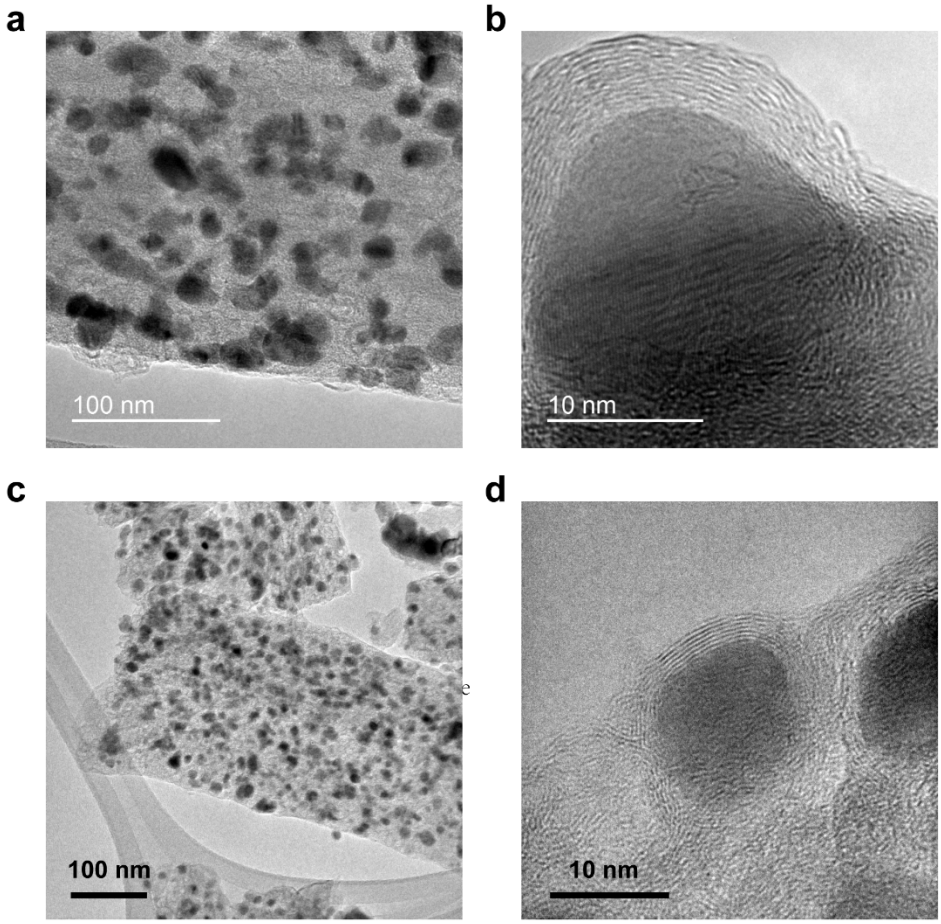

Figure S21.

Characterization of CoN-GS and FeN-GS. TEM images of CoN-GS (a, b) and FeN-GS (c, d) catalysts, which present similar core-shell structures with NiN-GS.

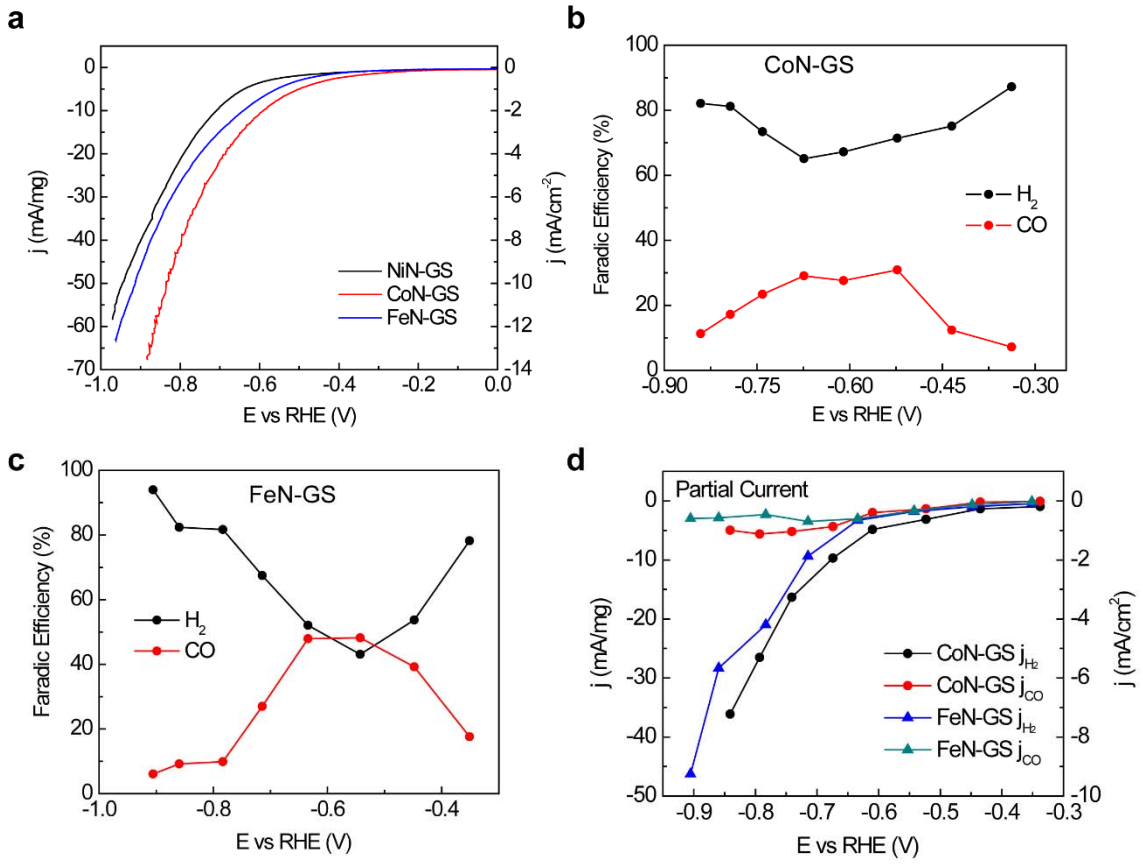

Figure S22.

Catalytic performances of CoN-GS and FeN-GS compared with NiN-GS. The highest CO FEs of Co and Fe catalysts are much lower than that of Ni, suggesting the specific Ni electronic structure involved in this highly selective CO_2 to CO conversion.

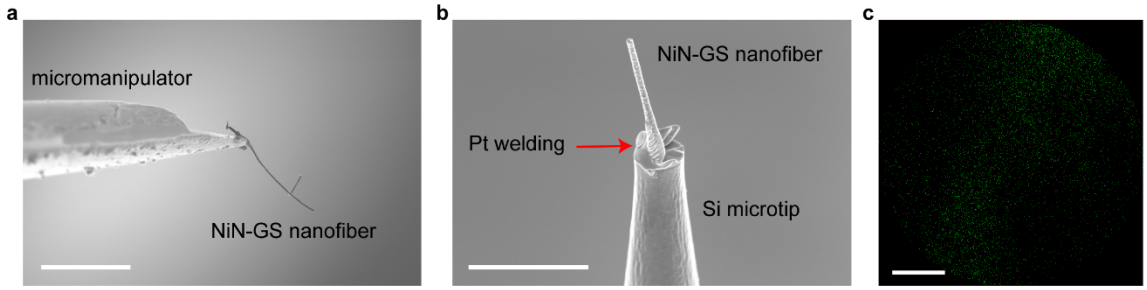

Figure S23.

The preparation of APT samples. (a) Transferring of the NiN-GS nanofiber using a micromanipulator. Scale bar: 10 μm. (b) One NiN-GS nanofiber was anchored onto a Si microtip using FIB and a micromanipulator. Scale bar: 5 μm. (**c**) The 2D Ni atom map of the selected area in Figure 3e. Scale bar: 5 nm.

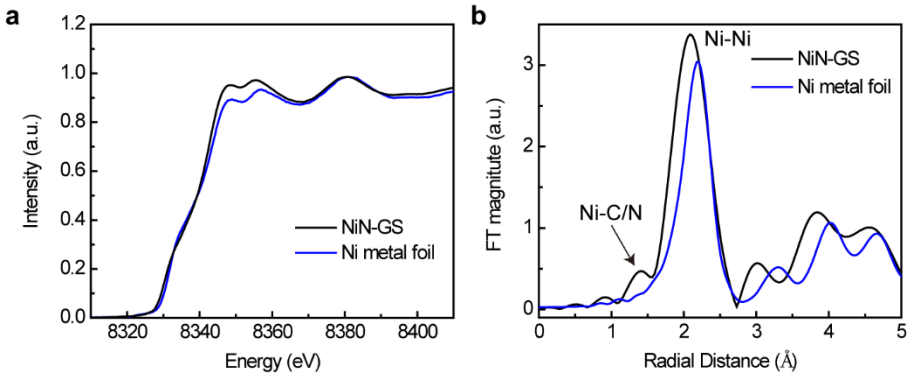

Figure S24

X-ray absorption spectroscopy of NiN-GS and Ni metal. Ni single atom coordination in graphene vacancies is observed as the small peak at ~ 1.4 Å.

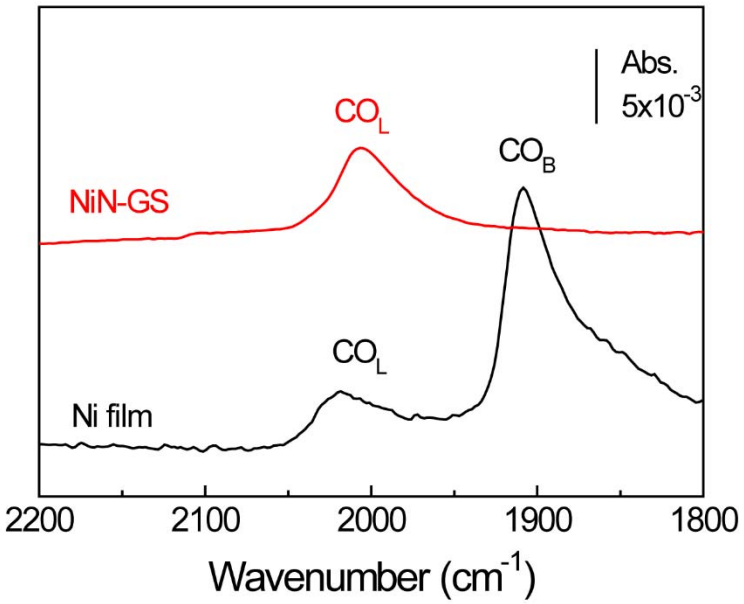

Figure S25

In situ electrochemical ATR-IR spectra of monolayer CO adsorption on NiN-GS and Ni film electrode. The surface Ni atomic sites distribution was further probed by comparing in situ ATR-IR spectra of CO adsorption on NiN-GS and Ni film electrode. The υ(CO) frequency is highly sensitive to its adsorption configuration.[27-28] The ATR-IR spectra of CO adsorption on Ni sites were taken in 0.1 M $NaClO_4$ at 0.0 V vs. RHE (pH ~ 6.9) with a spectral resolution of 2 cm^{-1}, where the reference spectra were taken in Ar-saturated 0.1 M $NaClO_4$ solution at a same potential prior to CO bubbling. The band at 1909 cm^{-1} is attributable to bridge-bonded CO (CO_B), while the band at 2007 or 2020 cm^{-1} to linear adsorbed CO (CO_L). It is noteworthy that the CO_B band feature is predominant over bulk Ni electrode, while CO_L is observed as the only adsorption mode on NiN-GS. The lacking of bridge-bonded CO footprint therefore suggests the single Ni atom dispersion predominates over the NiN-GS surface, in a good agreement with APT results.

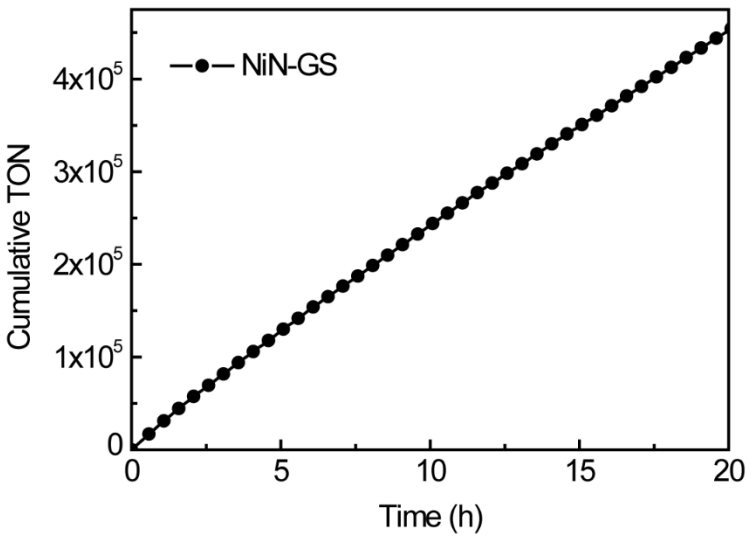

Figure S26.

The cumulative TON of CO_2 to CO conversion on the Ni active sites based on the electrolysis in Figure 2D. This nearly 'linear' shape suggests the excellent stability of the active sites.

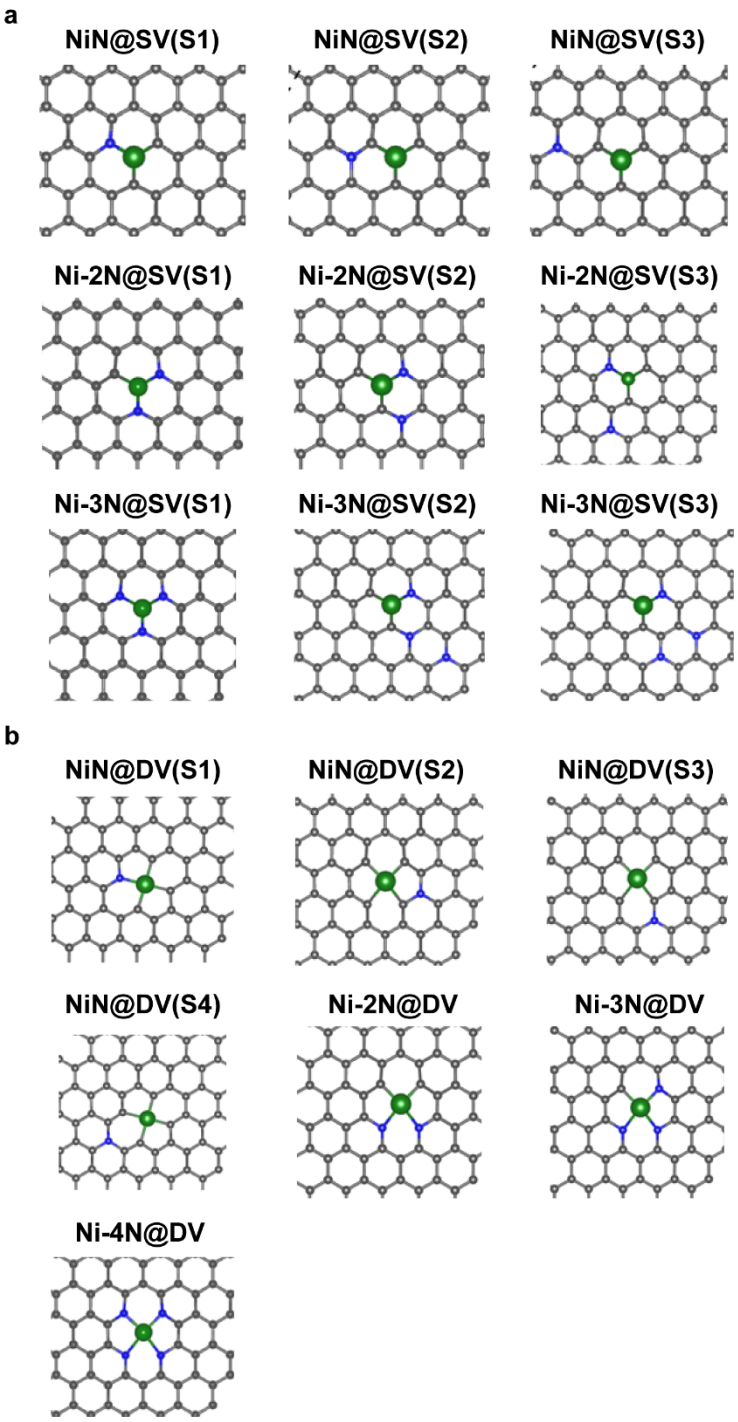

Figure S27.

Different N configurations in Ni@SV (a) and Ni@DV (b). Color code, C: gray, Ni: green, N: blue.

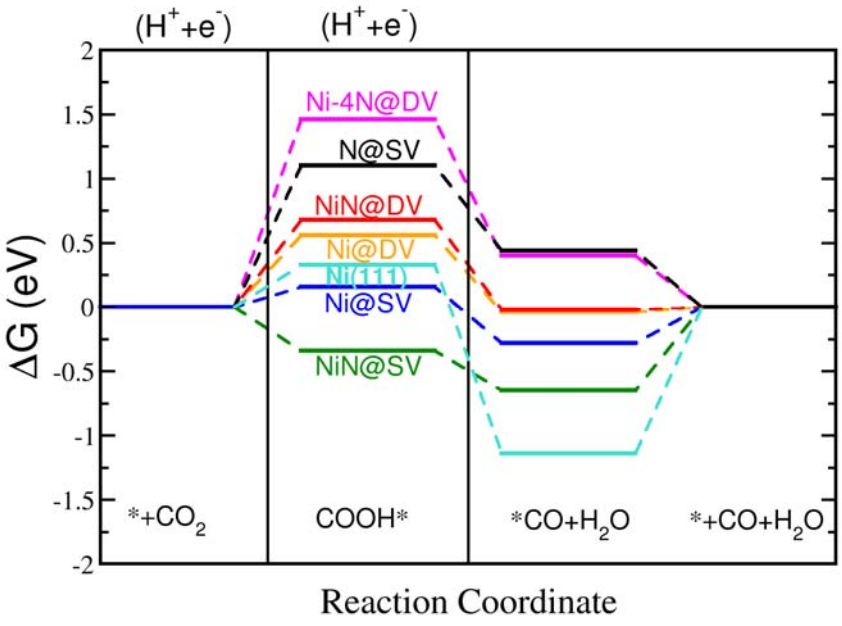

Figure S28.

The free energy diagram of CO_2 to CO conversion on different atomic sites under equilibrium potential of – 0.12 V vs. RHE with solvation correction.

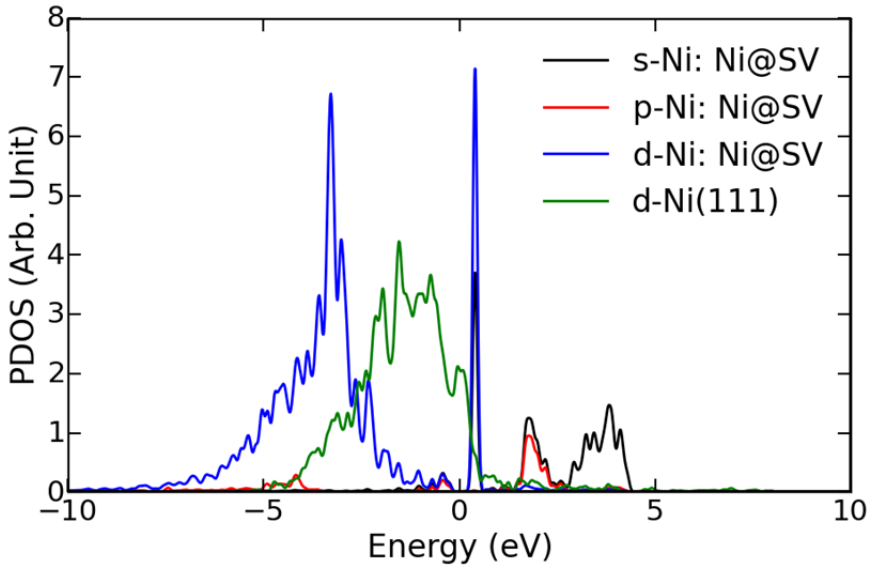

Figure S29.

Projected density of states (PDOS) for the Ni atom in Ni@SV and the Ni surface atom on Ni(111). After electronic hybridization with carbon atoms in graphene layer, Ni@SV exhibits an opened gap between occupied and unoccupied states in contrast to those of Ni(111). The unoccupied states shown as the narrow peak at ~ 1 eV above Fermi energy (E_f) originates from the hybridization of the in-plane d-states of Ni with the sp^2-states of its neighboring C atoms. In fact, not only d-states, but also s- and p-states of Ni contribute to the hybridization and form sharp peaks close to the Fermi level, indicating a strong Ni-C bonding. The most important asset of the Ni@SV system is the presence of much higher PDOS around E_f than that found in Ni(111). Indeed, these states are those responsible for the marginally different catalytic behavior of Ni-doped graphene. This phenomenon is known and has been reported for other transition metals in particular Au doped graphene [10, 29] as well as metal-functionalized porphyrin-like graphene.[30]

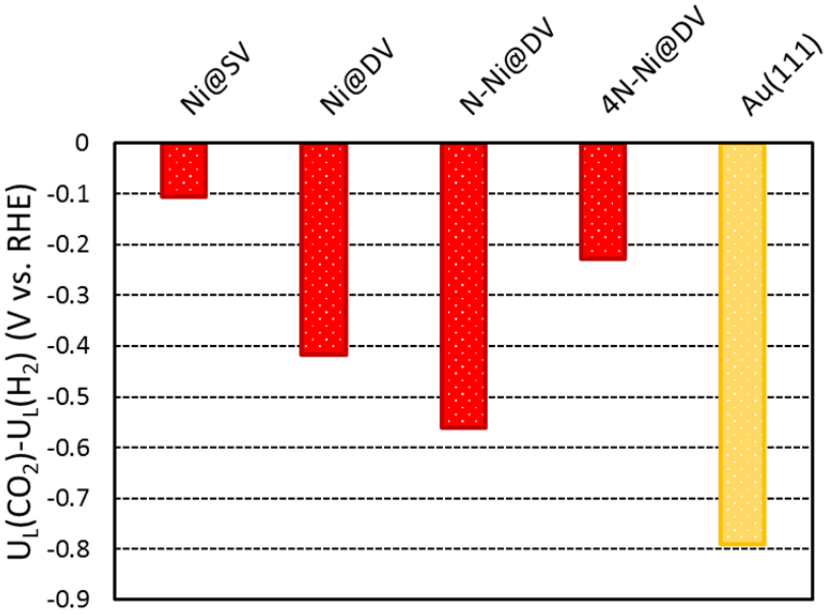

Figure S30.

Selectivity comparison between HER and CO_2RR on different Ni atomic sites in graphene. More positive $U_L(CO_2)$ - $U_L(H_2)$ corresponds to higher selectivity toward CO_2 reduction, in which Ni@SV is indicated as the most selective site. For the catalysts bind CO* strongly, the removal of CO* through CO* desorption will become the rate-limiting step. Therefore, instead of the Ni(111) and NiN@SV cases, we use this analysis only for the catalytic sites that bind CO* weakly, on which the formation of COOH* is expected to be the bottle neck step for CO production (*J. Phys. Chem. Lett.*, 2013, 4, 388).

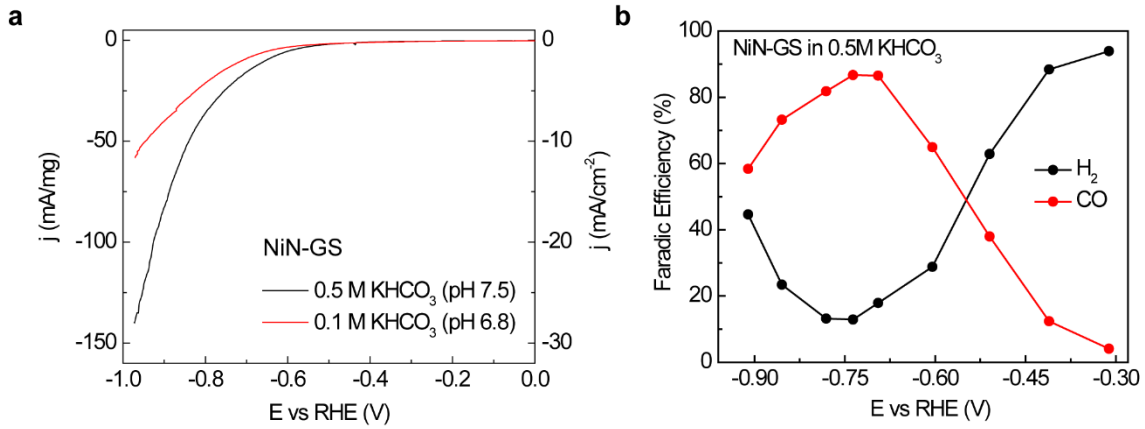

Figure S31.

Electrocatalytic CO_2 reduction performance of NiN-GS in 0.5 M $KHCO_3$ solutions. The highest CO FE is ~ 87 % under – 0.74 V vs RHE (- 0.62 V overpotential), with a current density of ~ 5 mA/cm^2 under a mass loading of 0.2 mg/cm^2.

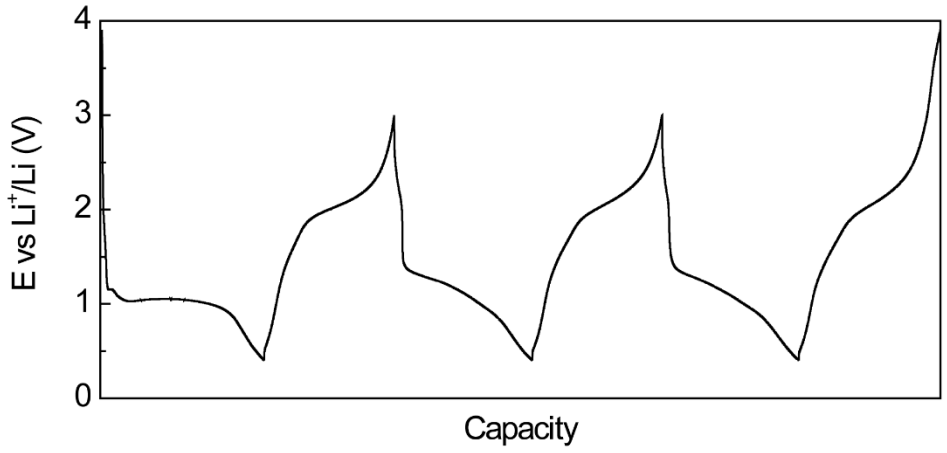

Figure S32.

The galvanostatic cycling profile of Co_3O_4 NPs on CFP electrode. The Li^+ charging and discharging process helps to create active boundaries and surface areas in Co_3O_4 catalysts.

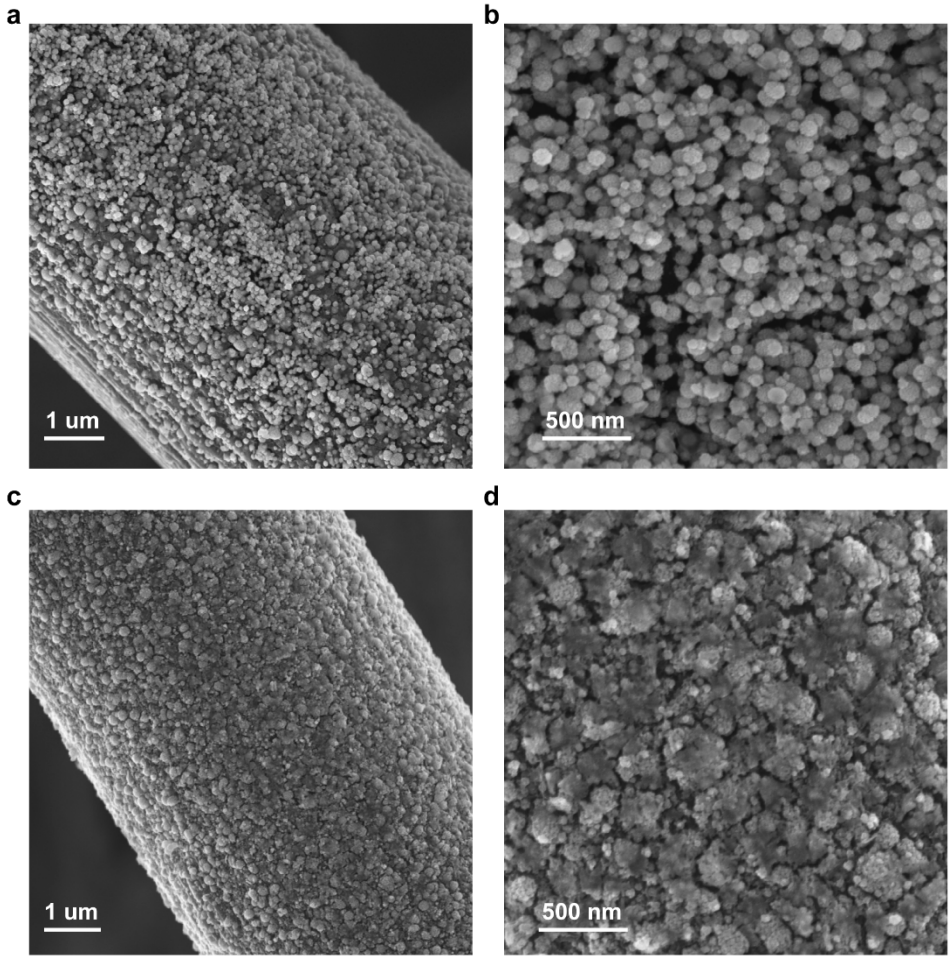

Figure S33.

SEM images of Co_3O_4 NPs before (a, b) and after (c, d) the Li^+ tuning process. The NP grains became much smaller after the tuning process.

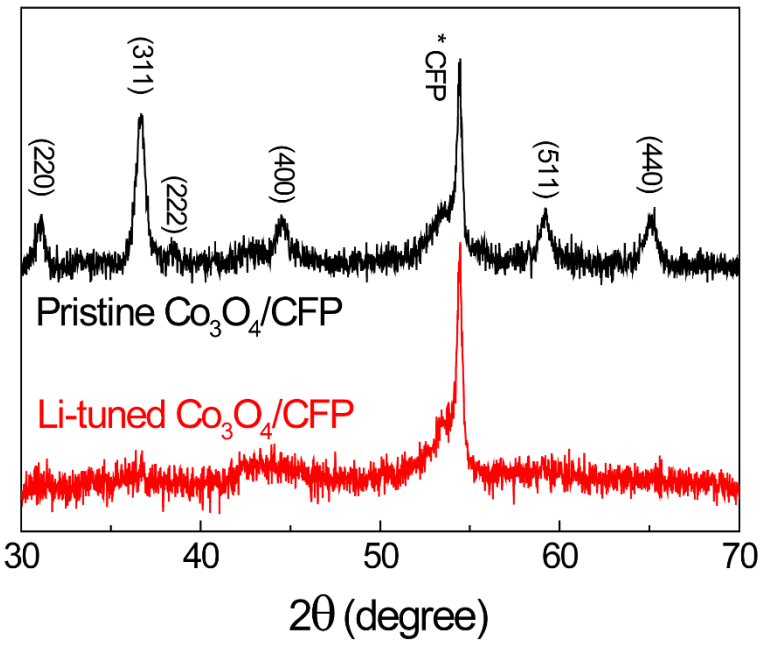

Figure S34.

XRD patterns of Co_3O_4 and Li-Co_3O_4. No peaks can be detected after the Li tuning process, suggesting the ultra-small NPs created by the tuning method.

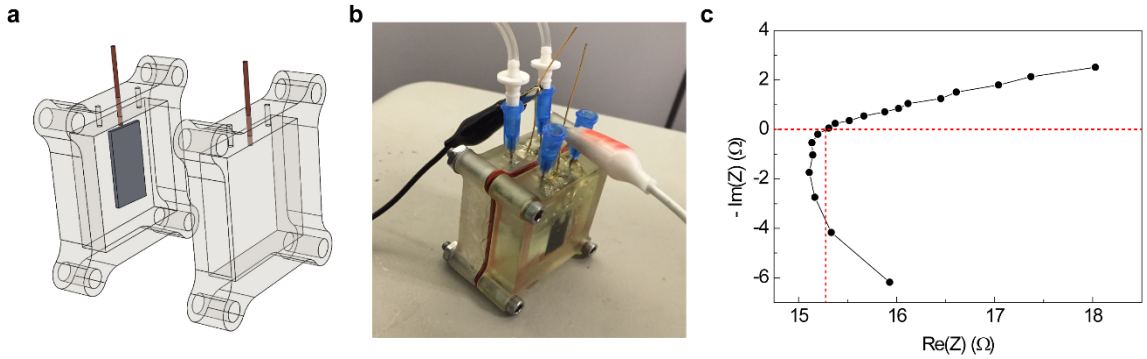

Figure S35.

The 3D-printed electrosynthetic cell for artificial photosynthesis. The design of this two-electrode cell instead of the traditional H-cell is to minimize the electrode distance and thus the iR loss. (**a**) An expanded view of the 3D-printed cell. (**b**) A photograph of the 3D-printed electrosynthetic cell. The cathodic chamber is filled with 0.5 M $KHCO_3$ and the anodic is 0.5 M $KHCO_3$ + 0.5 M K_2HPO_4/KH_2PO_4 buffer solution. The pH is balanced at 7.5 under CO_2 saturation. The cathode catalyst is NiN-GS for CO_2 reduction to CO, and anode catalyst is Li-Co_3O_4 for OER. (**c**) The solution resistance across the two electrodes was measured to be ~ 15 Ω.

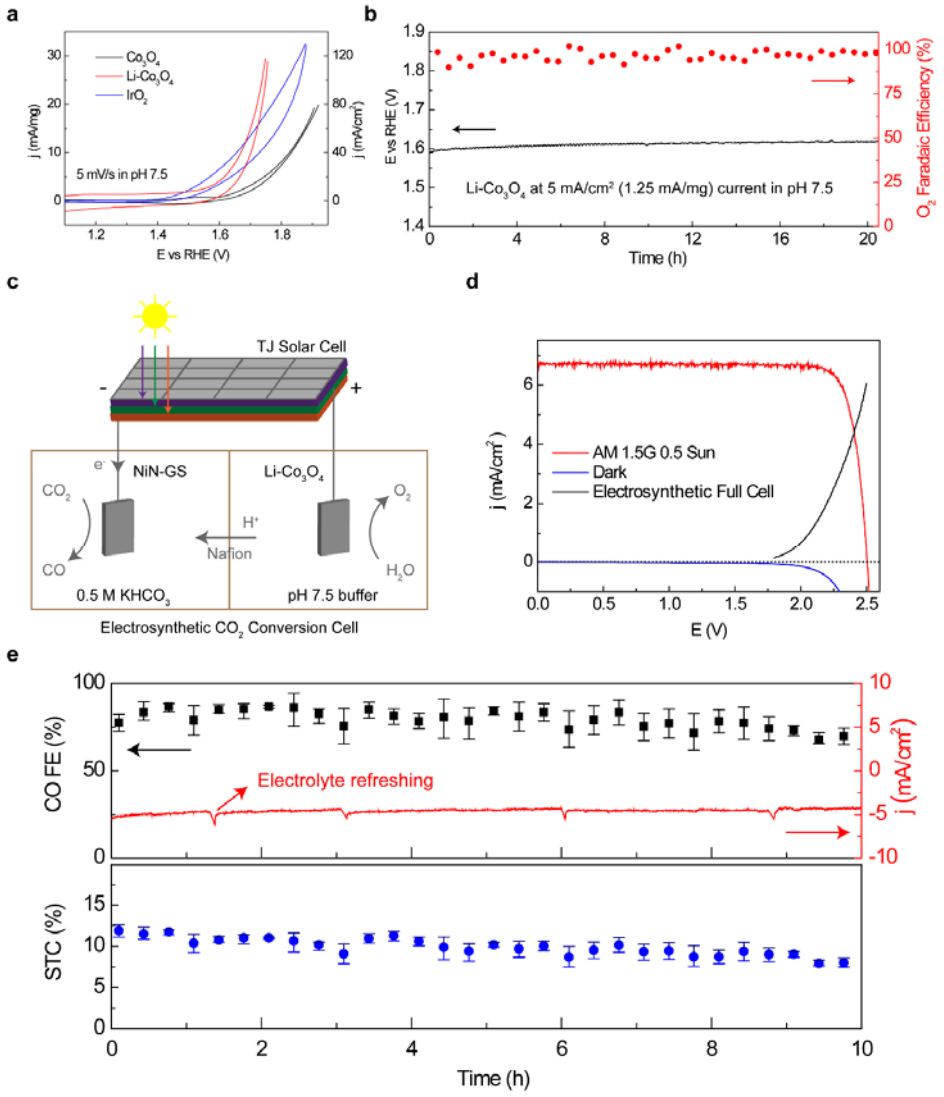

Figure S36.

Solar to CO artificial photosynthesis. (a) OER CVs of pristine Co_3O_4, Li-Co_3O_4, and IrO_2 at a scan rate of 5 mV/s in pH 7.5 solution. The catalyst loading is 4 mg/cm^2 on carbon fiber papers. The OER catalytic activity of Co_3O_4 NPs after Li^+ tuning is significantly improved, which performs even better than the benchmark IrO_2 under high current densities. (b) Long-term OER stability and O_2 FE test of Li-Co_3O_4 under 5 mA/cm^2 current. The potential to deliver this current is maintained at ~ 1.6 V vs RHE for more than 20 h with negligible degradation. (c) Schematic of the artificial photosynthesis system. The TJ solar cell and the electrosynthetic cell is directly wired together. The solar illumination was tuned to AM 1.5G 0.5 Sun to match the electrocatalytic current. (d) I-V curves of the 1 cm^2 TJ solar cell under AM 1.5G 0.5 Sun illumination and in the dark, with the electrosynthetic full cell I-V curve overlapped. The point of intersection represents the working status of the artificial photosynthesis system. (e) Around 10 % artificial photosynthesis efficiencies were achieved by earth-abundant electrocatalysts. The overall current remains stable at ~ 4.5 mA/cm^2.

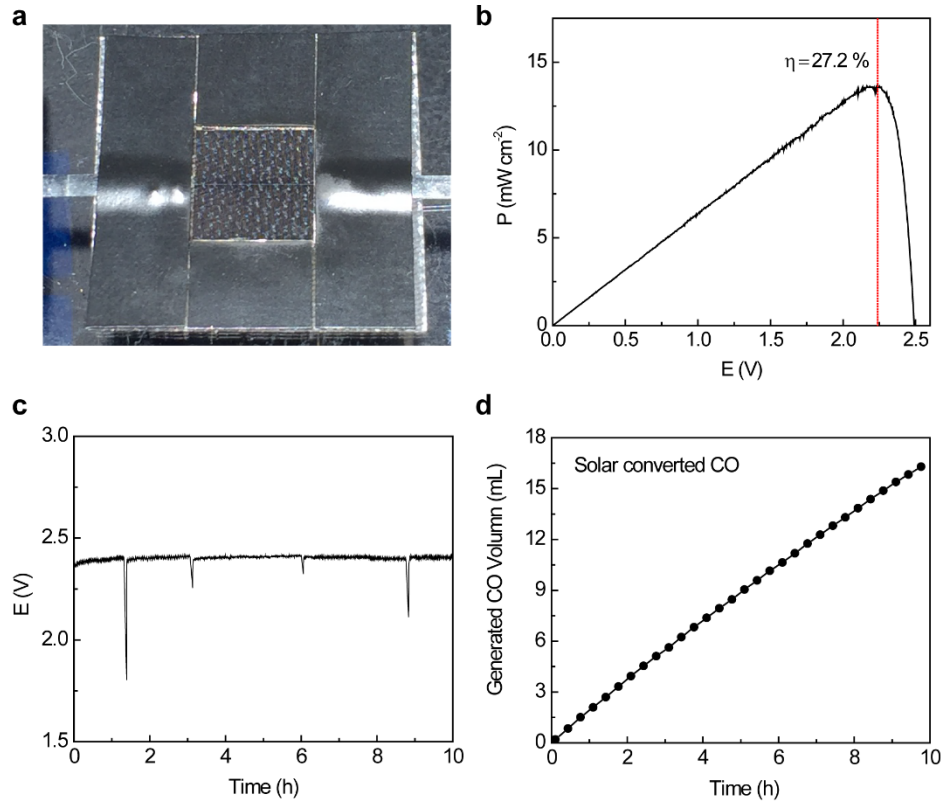

Figure S37.

Additional demonstration on solar to fuel conversion. (a) Photograph of TJ solar cell. (b) P-V curve of the TJ solar cell, with a maximal solar to electricity efficiency of 27.2 % under AM 1.5G 0.5 Sun illumination. (c) The solar cell voltage remains stable at ~ 2.4 V. (d) The accumulated CO volume during the 10-h continuous artificial photosynthesis.

Supplemental Tables

	Overpotential (V)	H_2 FE (%)	CO FE (%)	j_{CO} (mA/ mg)	TOF of CO (s^{-1})
0.1 M $KHCO_3$ GC electrode	0.23	97	4	-2.7×10^{-2}	1.1×10^{-2}
	0.33	84.8	8.1	-7.9×10^{-2}	3.2×10^{-2}
	0.43	75	16.2	-3.0×10^{-1}	1.2×10^{-1}
	0.52	50.6	42.5	-1.6	6.4×10^{-1}
	0.59	39.8	63.2	-6.3	2.6
	0.63	21.5	81.8	-10.8	4.5
	0.66	15.1	85.9	-16.1	6.6
	0.70	12.6	93.2	-19.4	8.0
	0.74	24.3	77	-20.4	8.4
	0.80	40.8	59.6	-20.7	8.5
	0.86	61.2	39.1	-17.2	7.1
0.5 M $KHCO_3$ GC electrode	0.57	17.9	86.5	-13.0	5.2
	0.62	12.9	86.7	-18.9	7.6
1.0 M $KHCO_3$ GDL electrode	0.27	13.0	5.8	-1.6	6.6×10^{-1}
	0.32	16.2	15.9	-4.7	1.9
	0.37	35.2	62.3	-19.3	8.0
	0.48	8.9	86.7	-31.4	12.9
	0.57	11.6	90.7	-40.1	16.5
	0.66	16.1	91.9	-49.1	20.2
	0.75	28.6	79.8	-53.9	22.2
	0.83	49.2	57.3	-50.4	20.8

Table S1

The CO_2RR performances of NiN-GS on glassy carbon (GC) and gas diffusion layer (GDL) electrodes in H-cell and Flow-cell respectively, with different concentrations of $KHCO_3$ electrolytes. The catalyst mass loadings are 0.2 mg/cm^2.

Catalyst	j (mA/mg)	Mass loading (mg/cm^2)	Overpotential (V)	Electrolyte	CO FE (%)	TOF (s^{-1})	Reference
NiN-GS	20.8	0.2	0.70	0.1M $KHCO_3$	93.2	8.0	This work
NiN-GS	21.3 (mA/cm^2)	1.0	0.64	0.5M $KHCO_3$	96.0	8.5	This work
NiN-GS	36.2	0.2	0.48	1M $KHCO_3$	86.7	12.9	This work
NiN-GS	53.4	0.2	0.66	1M $KHCO_3$	91.9	20.2	This work
COF-367-Co (1%) (Co porphyrin)	1.35	0.33	0.55	0.5M $KHCO_3$	53	2.6	*Science* **349**, 1208 (2015)
COF-367-Co	13.2	0.25	0.55	0.5M $KHCO_3$	91	0.53	*Science* **349**, 1208 (2015)
CoPc/CNT (2.5%)	25.0	0.4	0.51	0.1M $KHCO_3$	92	2.7	*Nat. Commun.* **8**, 14675 (2017)
Au NWs	1.84	4.4 (Au)	0.23	0.5M $KHCO_3$	94	0.02[a]	*JACS* **136**, 16132 (2014)
Au needles	4.4	3.4	0.24	0.5M $KHCO_3$	95	0.04[b]	*Nature* **537**, 382 (2016)
Au foil	5.0 (mA/cm^2)	N/A (bulk foil)	0.59	0.5M $KHCO_3$	87.1	4.9[b]	*Chem. Lett.* **14**, 1695 (1985)
Nanoporous Ag	1.1	16	0.49	0.5M $KHCO_3$	92.1	0.002[a]	*Nat. Commun.* **5**, 3242 (2014)
Ag foil	5.0 (mA/cm^2)	N/A (bulk foil)	0.90	0.5M $KHCO_3$	75.7	4.2[b]	*Chem. Lett.* **14**, 1695 (1985)
FeMn-N-C	1.8	0.785	0.4	0.1M $KHCO_3$	84	N/A	*Angew* **54**, 10758 (2015)
Ni-N-Gr	2	0.3	0.58	0.1M $KHCO_3$	90	0.75	*Small* **12**, 6083 (2016)
Ni_2-CPDpy973(1)	10	0.055	0.78	0.1M $KHCO_3$	87	N/A	*Nat. Commun.* **8**, 109 (2017)

[a] Numbers obtained from Ref. [31].

[b] The site density is obtained from the standard metal surface site density multiplied by the roughness factor.

Table S2

Comparisons of NiN-GS catalyst with reported state-of-the-art high-performance CO_2-to-CO electrocatalysts in aqueous solutions.

Configuration	ΔE_f (eV)	Configuration	ΔE_f (eV)
Ni@SV	-2.33	**Ni@DV**	-2.10
NiN@SV(S1)	0.42	NiN@DV(S1)	-0.66
NiN@SV(S2)	1.73	NiN@DV(S2)	0.53
NiN@SV(S3)	1.83	NiN@DV(S3)	0.99
Ni-2N@SV(S1)	0.70	NiN@DV(S4)	1.19
Ni-2N@SV(S2)	2.22	Ni-2N@DV	-1.45
Ni-2N@SV(S3)	2.21	Ni-3N@DV	-1.36
Ni-2N@SV(S4)	2.17	Ni-4N@DV	-1.38
Ni-3N@SV(S1)	1.18		
Ni-3N@SV(S2)	4.21		
Ni-3N@SV(S3)	4.28		

Table S3

The formation energies of the Ni@SV and Ni@DV were calculated using Eq. (a). Relative formation energies (relative to Ni@SV and Ni@DV respectively) of different N coordination in Ni@SV and Ni@DV structures were calculated using Eq. (b).

Configuration	ΔG_{CO} (eV)	ΔG_{COOH} (eV)	Configuration	ΔG_{CO} (eV)	ΔG_{COOH} (eV)
Ni@SV	0.02	0.58	**Ni@DV**	0.20	0.98
NiN@SV(S1)	-0.41	0.07	NiN@DV(S1)	0.22	1.10
NiN@SV(S2)	-0.25	0.43	NiN@DV(S2)	0.01	1.00
NiN@SV(S3)	-0.17	0.45	NiN@DV(S3)	0.12	1.03
Ni-2N@SV(S1)	-0.77	0.11	NiN@DV(S4)	0.00	0.81
Ni-2N@SV(S2)	-0.63	0.13	Ni-2N@DV	0.38	1.20
Ni-2N@SV(S3)	-0.55	0.24	Ni-3N@DV	0.68	1.23
Ni-2N@SV(S4)	-0.55	0.40	Ni-4N@DV	0.68	1.88
Ni-3N@SV(S1)	-1.24	-0.27			
Ni-3N@SV(S2)	-0.77	0.12			
Ni-3N@SV(S3)	-0.56	0.41			

Table S4

Calculated adsorption energies of *CO (ΔG_{CO}) and *COOH (ΔG_{COOH}) as reaction intermediates on different atomic configurations at U = 0.0 V *vs*. RHE.

Configuration	ΔG_H (eV)	Configuration	ΔG_H (eV)
Ni@SV	0.50	**Ni@DV**	0.56
NiN@SV(S1)	0.52	NiN@DV(S1)	0.53
NiN@SV(S2)	0.13	NiN@DV(S2)	-0.42
NiN@SV(S3)	0.27	NiN@DV(S3)	-0.40
Ni-2N@SV(S1)	-0.07	NiN@DV(S4)	-0.53
Ni-2N@SV(S2)	-0.02	Ni-2N@DV	0.86
Ni-2N@SV(S3)	0.01	Ni-3N@DV	1.03
Ni-2N@SV(S4)	-0.00	Ni-4N@DV	1.65
Ni-3N@SV(S1)	-0.13		
Ni-3N@SV(S2)	0.05	**Ni (111)**	-0.26
Ni-3N@SV(S3)	0.00		
NiN@SV(S1)	-0.02		

Table S5

H adsorption energy on different atomic structures. HER is a competing reaction to the CO_2 reduction reaction in aqueous solutions. The free energy of adsorbed H (ΔG_H) is known to be a good descriptor of the HER activity. Herein, we calculated the Both Ni@SV and Ni@DV present weak H binding which indicates a poor HER activities. Under a large enough overpotential, HER can compete CO_2 reduction and take over the reaction again.

Atomic Sites	ΔG_{CO*}	ΔG_{H}
Ni@SV	0.02	0.47
Ni@DV	0.20	0.56
Co@SV	-0.13	-0.24
Co@DV	-0.51	0.21

Table S6

Simulations of CO desorption and HER on Co and Ni atomic sites. While the Co atomic sites bind CO stronger than Ni, they present better HER catalytic activities.

References:

1 Huo, S.-J., Wang, J.-Y., Yao, J.-L. and Cai, W.-B. (2010). Exploring electrosorption at iron electrode with in situ surface-enhanced infrared absorption Spectroscopy. Anal. Chem. *82*, 5117-5124.

2 Jiang, K., Wang, H., Cai, W.-B. and Wang, H. (2017). Li electrochemical tuning of metal oxide for highly selective CO2 reduction. ACS Nano *11*, 6451-6458.

3 Jhong, H.-R. M., Brushett, F. R. and Kenis, P. J. A. (2013). The effects of catalyst layer deposition methodology on electrode performance. Adv. Energy Mater. *3*, 589-599.

4 Ramkumar, J. and Mukherjee, T. (2007). Role of ion exchange in permeation processes. Talanta *71*, 1054-1060.

5 Giannozzi, P., Baroni, S., Bonini, N., Calandra, M., Car, R., Cavazzoni, C., Ceresoli, D., Chiarotti, G. L., Cococcioni, M., Dabo, I., et al. (2009). QUANTUM ESPRESSO: a modular and open-source software project for quantum simulations of materials. J. Phys. Condens. Matter *21*, 395502.

6 Bahn, S. R. and Jacobsen, K. W. (2002). An object-oriented scripting interface to a legacy electronic structure code. Comput. Sci. Eng. *4*, 56-66.

7 Adllan, A. A. and Dal Corso, A. (2011). Ultrasoft pseudopotentials and projector augmented-wave data sets: application to diatomic molecules. J. Phys. Condens. Matter **23**, 425501.

8 Wellendorff, J., Lundgaard, K. T., Mogelhoj, A., Petzold, V., Landis, D. D., Norskov, J. K., Bligaard, T. and Jacobsen, K. W. (2012). Density functionals for surface science: Exchange-correlation model development with Bayesian error estimation. Phys. Rev. B 85, 235149.

9 Monkhorst, H. J. and Pack, J. D. (1976). Special points for Brillouin-zone integrations. Phys. Rev. B *13*, 5188.

10 Krasheninnikov, A. V., Lehtinen, P. O., Foster, A. S., Pyykkö, P. & Nieminen, R. M. (2009). Embedding transition-metal atoms in graphene: structure, bonding, and magnetism. Phys. Rev. Lett. *102*, 126807.

11 Norskov, J. K., Rossmeisl, J., Logadottir, A., Lindqvist, L., Kitchin, J. R., Bligaard, T. and Jonsson, H. (2004). Origin of the overpotential for oxygen reduction at a fuel-cell cathode. J. Phys. Chem. B *108*, 17886-17892.

12 Chen, J., Li, C. and Shi, G. (2013). Graphene Materials for Electrochemical Capacitors. J. Phys. Chem. Lett. *4*, 1244-1253.

13 Xia, J., Chen, F., Li, J. and Tao, N. (2009). Measurement of the quantum capacitance of graphene. Nat. Nanotech. *4*, 505-509.

14 Wang, H., Lee, H.-W., Deng, Y., Lu, Z., Hsu, P.-C., Liu, Y., Lin, D. and Cui, Y. (2015). Bifunctional non-noble metal oxide nanoparticle electrocatalysts through lithium-induced conversion for overall water splitting. Nat. Commun. *6*, 7261.

15 Zhang, B., Zheng, X. L., Voznyy, O., Comin, R., Bajdich, M., Garcia-Melchor, M., Han, L. L., Xu, J. X., Liu, M., Zheng, L. R., et al. (2016). Homogeneously dispersed, multimetal oxygen-evolving catalysts. Science, *352*, 333-337.

16 Cheng, Y. and Jiang, S. P. (2015). Advances in electrocatalysts for oxygen evolution reaction of water electrolysis-from metal oxides to carbon nanotubes. Prog. Nat. Sci. Mater. Inter. *25*, 545-553.

17 Zhao, Y. F., Chen, S. Q., Sun, B., Su, D. W., Huang, X. D., Liu, H., Yan, Y. M., Sun, K. N. and Wang, G. X. (2015). Graphene-Co3O4 nanocomposite as electrocatalyst with high performance for oxygen evolution reaction. Sci. Rep. *5*, 7629.

18 Lu, X. F., Liao, P. Q., Wang, J. W., Wu, J. X., Chen, X. W., He, C. T., Zhang, J. P., Li, G. R. and Chen, X. M. (2016). An alkaline-stable, metal hydroxide mimicking metal–organic framework for efficient electrocatalytic oxygen Evolution. J. Am. Chem. Soc. *138*, 8336-8339.

19 Liu, C., Colón, B. C., Ziesack, M., Silver, P. A. and Nocera, D. G. (2016). Water splitting–biosynthetic system with CO2 reduction efficiencies exceeding photosynthesis. Science *352*, 1210-1213.

20 Kanan, M. W. and Nocera, D. G. (2008). In situ formation of an oxygen-evolving catalyst in neutral water containing phosphate and Co2+. Science *321*, 1072-1075.

21 Schreier, M., Curvat, L., Giordano, F., Steier, L., Abate, A., Zakeeruddin, S. M., Luo, J., Mayer, M. T. and Grätzel, M. (2015). Efficient photosynthesis of carbon monoxide from CO2 using perovskite photovoltaics. Nat. Commun. *6*, 7326.

22 Jia, J. Y., Seitz, L. C., Benck, J. D., Huo, Y. J., Chen, Y. S., Ng, J. W. D., Bilir, T., Harris, J. S. and Jaramillo, T. F. (2016). Solar water splitting by photovoltaic-electrolysis with a solar-to-hydrogen efficiency over 30%. Nat. Commun. *7*, 13237.

23 Blankenship, R. E., Tiede, D. M., Barber, J., Brudvig, G. W., Fleming, G., Ghirardi, M., Gunner, M. R., Junge, W., Kramer, D. M., Melis, A., et al. (2011). Comparing photosynthetic and photovoltaic efficiencies and recognizing the potential for improvement. Science *332*, 805-809.

24 Jussila, H., Yang, H., Granqvist, N. and Sun, Z. (2016). Surface plasmon resonance for characterization of large-area atomic-layer graphene film. Optica *3*, 151-158.

25 Moulder JF, S. W., Sobol PE, Bomben KD. (1995). Handbook of X-ray Photoelectron Spectroscopy. ULVAC-PHI, Inc., Chigasaki, Japan; Physical Electronics USA, Inc, Chanhassen, MN.

26 Somorjai, G. A. (1981). Chemistry in Two Dimensions: Surfaces. (Cornell University Press).

27 Qiao, B. T., Wang, A. Q., Yang, X. F., Allard, L. F., Jiang, Z., Cui, Y. T., Liu, J. Y., Li, J. and Zhang, T. (2011). Single-atom catalysis of CO oxidation using Pt1/FeOx. Nat. Chem. *3*, 634-641.

28 Mojet, B. L., Ebbesen, S. D. and Lefferts, L. (2010). Light at the interface: the potential of attenuated total reflection infrared spectroscopy for understanding heterogeneous catalysis in water. Chem. Soc. Rev. *39*, 4643-4655,

29 Rodríguez-Manzo, J. A., Cretu, O. and Banhart, F. (2010). Trapping of metal atoms in vacancies of carbon nanotubes and graphene. ACS Nano *4*, 3422-3428.

30 Tripkovic, V., Vanin, M., Karamad, M., Bjorketun, M. E., Jacobsen, K. W., Thygesen, K. S. and Rossmeisl, J. (2013). Electrochemical CO2 and CO reduction on metal-functionalized porphyrin-like graphene. J. Phys. Chem. C *117*, 9187-9195.

31 Zhang, X., Wu, Z. S., Zhang, X., Li, L. W., Li, Y. Y., Xu, H. M., Li, X. X., Yu, X. L., Zhang, Z. S., Liang, Y. Y., et al. (2017). Highly selective and active CO2

reduction electrocatalysts based on cobalt phthalocyanine/carbon nanotube hybrid structures. Nat. Commun. *8*, 14675.